Vortex-induced vibrations of a cantilevered blunt plate: POD of TR-PIV measurements and structural modal analysis

Yann Watine, Céline Gabillet, Boris Lossouarn, Jean-François Deü, Jacques-André Astolfi

Vortex induced vibrations analysis of a cantilevered blunt plate by propper orthogonal decomposition of TR-PIV and structural modal analysis

Yann Watine[a,*], Céline Gabillet[a], Boris Lossouarn[b], Jean-François Deü[b], Jacques-André Astolfi[a]

[a] *Institut de Recherche de l'Ecole Navale (IRENav), EA 3634 - Ecole Navale, 29240, Brest, France.*
[b] *Laboratoire de Mécanique des Structures et des Systèmes Couplés (LMSSC), Conservatoire national des arts et métiers (Cnam), 292 rue Saint-Martin, 75 003, Paris, France.*

Abstract

Vortex induced vibrations sustained by immersed bodies may induce early structural fatigue and acoustic noise radiation. The present study consists in an experimental characterization of the vortex shedding and induced vibrations of a cantilevered blunt rectangular aluminium plate of chord to thickness ratio 16.7, immersed in a uniform water flow in the hydrodynamic tunnel of the French Naval Academy Research Institute. Experiences have been conducted at zero degrees incidence for Reynolds numbers Re_c (based on chord length) ranging from 2.5×10^5 to 9.5×10^5, leading to turbulent wake conditions. The hydrodynamic properties of the wake have been evaluated by statistical analysis, Proper Orthogonal Decomposition and vortex core identification of Time Resolved Particle Image Velocimetry fields. The structural response of the plate has been examined by laser vibrometry through modal analysis. The fluid-structure interactions have been examined for three different vibration regimes: out of resonance, lock-off resonance with the 1^{st} twisting mode and lock-in resonance. In the out of resonance regime, the strength of the Karman vortices is preferentially controlled by the Strouhal number. At the lock-in, it has been observed that there is an energy transfer in the wake from low order energetic modes to high order energetic modes. In particular,the flapping of the separated shear layer at the lock-in is responsible for an enhancement of the contributions to the total kinetic energy of both the wake bubble's instability and the Karman vortices. The flapping seems to be also responsible for the occurrence of the resonance at a reduced velocity, smaller than the reduced velocity of the lock-in.

Keywords: Vortex induced vibration, modal decomposition, TR-PIV, POD

1. Introduction

Separated and reattached turbulent flows are commonly found in numerous engineering applications such as flows over hydrofoils, ship propellers or pump blades. They are encountered in flows around bodies of important chord to thickness ratio. For these kind of flows, the coupling between the leading edge separation and the shedding vortices in the wake is much more complex than in strong separated flows. When fluid-structure coupling occurs, the physical understanding and the modelling of these kinds of flows are still challenging. The phenomenon of vortex shedding from elongated and bluff bodies has received increasing attention over the years. It is well described by the non-dimensional Strouhal number $St_L = \frac{f_{vs}.L}{U_\infty}$, which is a scaling of the vortex shedding frequency f_{vs}, using a representative length L of the body and the upstream velocity U_∞. The Strouhal number is known to be linked with the Reynolds number $Re_L = \frac{U_\infty.L}{\nu}$. For elongated bodies, there is a discrepancy between Strouhal number values according to the Reynolds number, but also according to the type of edge (leading/trailing edges) as well as the thickness ratio, Rostani et al.

*Corresponding author
Email address: yann.watine@ecole-navale.fr (Yann Watine)

(2019) [1]. Indeed, the Strouhal number is very sensitive to the nature of the boundary shear layers and it can vary with the chord to thickness ratio c/D. For a flat plate with sharp edges, the Reynolds number has a noticeable influence on the Strouhal number for small angles of attack at which flow reattachment occurs. The influence of the Reynolds number is weak at large incidence angles for which the boundary layer is fully separated, Chen and Fang (1996) [2].

For plates of square leading and trailing edges, Stokes and Welsh (1986) [3] have summarized the results obtained by Parker and Welsh (1983) [4] and defined four different vortex shedding regimes depending on the ratio c/D. These regimes were confirmed by Shi et al.(2010) [5] and by Zhang et al. (2015) [6] for flat plates with c/D ranging from 1 to 9 at a thickness-based Reynolds numbers $Re_D = 1 \times 10^3$. For short plates ($c/D < 3.2$), the flow separation occurs at the leading-edge corner and there is a direct interaction of the shear layer to generate a regular vortex street in the wake. For medium length plates ($3.2 < c/D < 7.6$), there is a reattachment of the shear layer to the trailing edge surface forming a regular vortex street in the wake. For long plates ($7.6 < c/D < 16$), the shear layer is always reattached upstream of the trailing edge and forms a separation bubble which grows and divides in a random manner. In this case, there is a random distribution of the vortices throughout the boundary layer. This produces irregular shedding and no clear regular vortex street. At last, for extra long plates ($16 > c/D$), the separation bubble fluctuates in length the same way as described in the previous case but the randomly distributed vortices diffuse before reaching the trailing edge. As a consequence, the fully developed turbulent shear layer induces a regular vortex street behind the plate which is not directly related to the formation of the leading edge separation bubble.

However, for Re_D from 1×10^3 to 3×10^3, Nakamura et al. (1991) [7] have put into light that the presence of a sharp trailing edge corner induces a somewhat different interpretation of vortex shedding. According to their study, the vortex shedding in the wake is influenced by the impinging shear layer instability for $3 < c/D < 15$. As a consequence, for this range of c/D values and for $Re_D = 1 \times 10^3$, they have established that the chord based Strouhal number St_c increases stepwise with increasing values of c/D and that the wavelength of the impinging shear layer instability is locked to the chord length. This phenomenon of impinging shear layer instability was also addressed by Naudascher and Rockwell (1994) [8] who concluded that for $c/D > 7$, it is rather vortex shedding by the separation bubble that interacts with the trailing edge vortex, thus leading to what is called the impinging leading edge vortex instability which is characterized by a feedback between the trailing edge shedding and the leading edge shedding through pressure waves. However, for $Re_D > 2 \times 10^3$ and $c/D > 12$, no trace of forcing by the shear layer or leading edge vortex induced instability has been evidenced in the wake by Nakamura et al. (1991) [7]. This is consistent with the fact that the dependency with c/D of the Strouhal number vanishes for $Re_D > 2 \times 10^3$ (Mills et al., 2003 [9]).

Taylor et al. (2014) [10] have investigated at high Reynolds numbers the influence on the trailing edge vortex shedding of a change in the length of the separation bubble by varying the geometry of the leading edge. For thickness-based Reynolds Re_D ranging from 4.0 to 7.5×10^4 and elongated bodies characterized by $c/D = 7$, they have demonstrated that there is no forcing by the impinging shear layer or leading edge vortex instability and that the Strouhal number, which is weakly dependent on the Reynolds number, strongly varies with the leading edge shape. A larger length of the leading edge separation-reattachment bubble, which is achieved for a square leading edge, plays in favour of a decrease in the Strouhal number.

In continuity of the researches of Strouhal (1915), studies of vortex induced vibrations rather focused on strong separated flows over bluff bodies. Blevins (1974) [11] explains that if a body periodically sheds vortices in its wake at a frequency near a harmonic of the natural frequency of the structure, vortex shedding may couple with the structural vibration. This phenomenon is known as lock-in and can generate vibration amplitudes hundreds of times higher than those caused by any other source. On the other hand, according to Griffin et al. (1974) [12] and Stansby (1976) [13], the mechanical vibrations of a body at the lock-in induces appreciable changes in the vortex shedding frequency and the range of Reynolds numbers where the vortex shedding frequency is locked to the structural natural frequency depends on the oscillation amplitude (Bearman (1984) [14]). Generally speaking, the larger the vibration amplitudes, the larger the Reynolds number range at lock-in. However, for bodies of large chord to thickness ratio, as observed by Toebes et al. (1961) [15], although severe vortex induced vibrations at lock-in may be confined into a narrow range of free stream velocity, resonant vibration amplitudes may persist over a wider range of free stream velocities.

For hydrofoils or plates of large chord to thickness ratio, vibrations at resonance and lock-in are very sensitive to the geometry of the trailing edge (Zobeiri et al. (2012) [16], Yao et al. (2014) [17]). Indeed, under lock-in conditions, Zobeiri (2012) [18] argues that the vibration amplitude of a hydrofoil trailing edge is so high, that its motion takes control of the instability mechanism that leads to vortex shedding and synchronizes the shedding frequency with the structural motion frequency. This comes from the fact that the lock in has a strong affinity with the torsional natural mode because it is the mode for which the wall displacement amplitude is maximised (Ausoni (2009) [19]). For this mode, the maxima displacement amplitude occurs at the leading and trailing edge meaning that the trailing edge motion is in phase along the entire span. As was observed by Toebes et al. (1961) [15], the variation of the vibration amplitude when changing the trailing edge geometry is mainly related to the differences in the degree to which the separating shear layers on both sides interacts with each other and the differences in the degree to which two-dimensionality of the early wake is preserved. It was assumed that the instability of the separation points at the trailing edge might contribute to a great extent to the vibrational behaviour. Indeed, lower vibrational amplitudes and a narrower range of free stream velocities at resonance were observed for plates designed in order to achieve fixed separation points at the trailing edge (made of re-entrant edges or square edges).

To conclude, it appears that studies of Fluid-Structure Interaction of elongated bodies with important chord to thickness ratio at high Reynolds numbers are missing in the literature survey. In particular, a detailed analysis is missing of the structure of the near wake according to the vibrations of the trailing edge. As said before, increasing the chord length c/D makes the system complex, as it is subjected to higher degrees of freedom, and so is also when increasing the Reynolds number. This study aims at characterizing the structure of the near wake of a blunt plate immersed at zero degrees of incidence in a uniform flow. The chord to thickness ratio c/D is 16.7, the chord-based Reynolds numbers Re_c are ranging into $[2.5 \times 10^5, 9.5 \times 10^5]$ and the thickness-based Reynolds number is varied in the range $[1.5 \times 10^4, 5.7 \times 10^4]$. In order to have a better control of the separating points, the leading and trailing edges are square. The structure of the near wake is characterized by PIV (Particle Image Velocimetry) and analysed with the use of POD (Proper Orthogonal Decomposition). Different types of POD modes are identified. The contribution of these POD structures is discussed according to the vibration regime of the plate (out of resonance, lock-off resonance and lock-in with the first twisting mode). The Von Karman vortices are identified and characterized by the Graftiaux method [20] and the evolution with the Reynolds number of their characteristics (size, strength, rotation rate) is analysed, according to the vibrational state of the plate. This article is complementary with the article of the authors (Watine et al. (2020) [21]). It provides deeper insight into the near-wake structure of the flow. The manuscript is organized as follows: in section 2, we introduce the experimental set-up and measurement techniques and in section 3 we present the analysis methods. In section 4 the vibrations of the structure under flow excitation are analysed and in section 5 we present the general features of the near wake and study the evolution of some of its statistical properties according to $\mathrm{Re_c}$. Section 6 presents the influence of Re_c on the properties of the Karman vortices. Finally in section 7, the POD decomposition of the near wake is used to discuss about the energetic contributions of different types of structures at the different vibration regimes. Section 8 is a discussion about the fluid structure interaction mechanism at resonance.

2. Experimental set-up and measurement techniques

The present section provides an exhaustive description of the experimental arrangement: hydrodynamic tunnel, geometry and materials of the structure as well as employed measurement techniques: laser vibrometry and time resolved particle image velocimetry (TR-PIV).

2.1. Hydrodynamic tunnel

Experiments were carried out in the hydrodynamic tunnel of the French Naval Academy Research Institute (IRENav). The test section is 1 m long with a 192 mm square section and is filled with water. The main flow turbulence intensity is reduced to 2% due to a honeycomb grid and a convergent section placed

upstream of the test section. The upstream velocity and the pressure at the entrance of the test section are controlled with an accuracy of 2% and 2.5% respectively. For the purpose of our study, the upstream velocity U_0 was varied from 2.5 to 9.5 m.s^{-1}. The pressure was adjusted to 1013 Pa. Refer to figure 1 for a general overview of the arrangement. Additional information about the tunnel can be found in Pernod et al. (2019) [22].

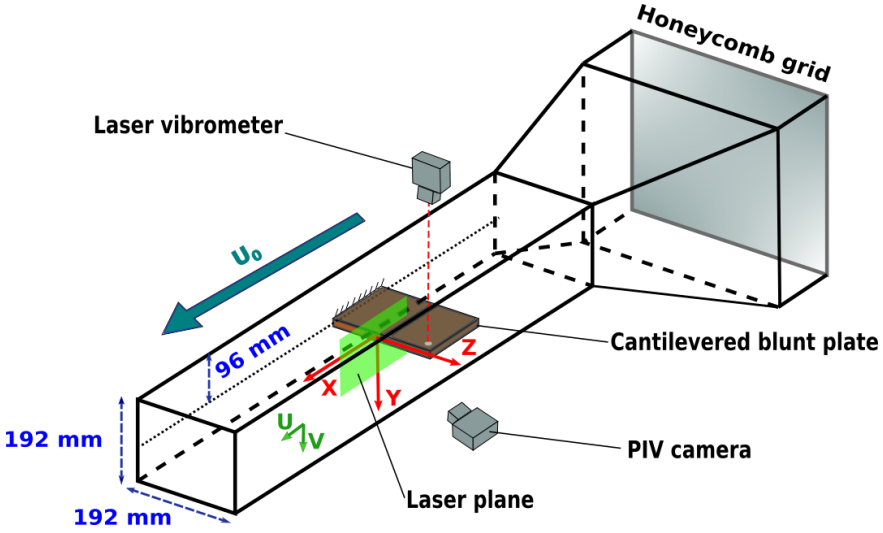

Figure 1: Test section of the IRENav hydrodynamic tunnel.

2.2. Structure geometry and materials

The tested structure consists of a blunt aluminium plate with a chord to thickness ratio c/D = 16.7 of mass M=0.38 kg. The span of the plate is s=191 mm, its chord is c=100 mm, and its thickness is D=6 mm. The plate mass to the fluid ratio $\frac{M}{\rho.D.s.c}$ is equal to 3.3. The plate is clamped at the backside of the test section by using an extension root. The clamped condition is considered as being applied at 50% of the chord. The plate is mounted in the test section with zero incidence, assuming a maximum uncertainty in the angle of attack of 0.1 °. The trailing edge at mid-thickness of the plate is chosen as the origin of the reference frame, x being the stream-wise direction, y being the downward vertical direction and z being the transverse direction, as shown in figure 1.

On each horizontal side of the plate there is a rectangular groove of dimension 61.5 mm × 71 mm × 1 mm intended to support two piezoelectric transducers on both sides. A thin layer of paraffin is added on top of the transducers to fill the residual depth of the cavity and reconstruct the surface in order to avoid added thickness and local roughness. The piezoelectric transducers are of the type P-876. A15 DuraAct patches supplied by PI Ceramic. Two of the four transducers can be used as an excitation source for the plate vibration, while the output of the two others can be used to control the vibration or as sensors to convert the mechanical displacement into a voltage signal. In the present work, only two transducers were used as a structural excitation source : they were power-supplied to characterize the natural frequencies and modal shapes of the plate, under still conditions. The vibration control, which is not the issue of the present paper, was not activated here and the remaining patches were connected in short-circuit. Figure 2 presents the geometry and dimensions of the aluminium flat plate.

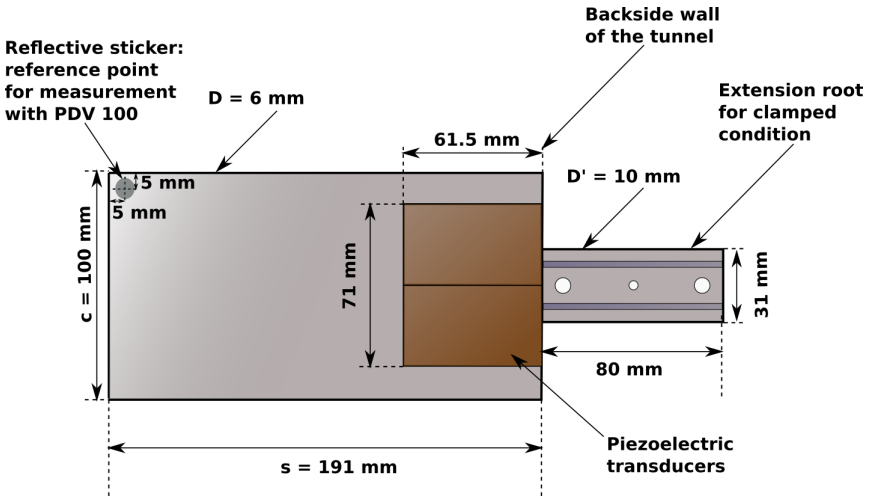

Figure 2: Geometry and dimension of the aluminium flat plate embedded with piezoelectric transducers.

2.3. Laser vibrometry

Laser vibrometry is a contactless vibration measurement method using the Doppler effect principle. Phase shift between the emitted and received laser signals provides characterization of the displacement velocity of the structure. The vibration measurements and associated modal analyses were performed with the Polytec® PDV-100 and PSV-400-B laser vibrometers. These instruments provided the mode shape associated to each natural frequency. Main specifications of the vibrometers are presented in table 1. Considering the fact that the bending and twisting mode amplitudes are maximal at the edges opposite to the clamping device, the reference point of PDV-100 measurement is achieved at 5 mm from the trailing edge on the upper side of the plate as shown in figure 2. In order to enhance the reflection of the laser beam at the reference point, a local reflective sticker has been added on the plate.

	PDV-100		**PSV-400-B**
Type	Single point	Type	Scanner
Laser type	HeNe	Laser type	HeNe
Laser wavelength	$\lambda = 633$ nm	Laser wavelength	$\lambda = 633\ nm$
Velocity range	$0.01 - 10$ m.s^{-1}	Velocity range	10 m.s^{-1}
Frequency range	$0.5 - 22$ kHz	Frequency range	40 kHz
Acquisition time	80 s	Angular resolution	$< 0.002°$/h
		Grid points spacing	25 mm

Table 1: Main technical specifications of the Polytec® PDV-100 and PSV-400-B laser vibrometers.

Mode shapes and natural frequencies were characterized in still air and in still water. This was made by analysing the vibration response to a white noise excitation provided by the two piezoelectric transducers consisting in a random succession of frequencies in a bandwidth of 0 to 2 kHz. The piezo alimentation tension was equal to 2 V. Figure 3 presents the vibratory frequency response function (FRF) of the plate to the piezoelectric voltage excitation in air and in water respectively at the reference point. The equation of the FRF corresponds to $\text{FRF} = \frac{\text{Velocity(m.s}^{-1})}{\text{Voltage(V)}}$ and its amplitude is expressed in decibels as $\text{FRF(dB)} = 20.\log(\frac{\text{FRF}}{\text{FRF}_{\text{reference}}})$ with $\text{FRF}_{\text{reference}} = 1$.

	Air	Water	Modal shape
First mode frequency f_1	60.95 Hz	25.65 Hz	Bending
Second mode frequency f_2	308.14 Hz	180.68 Hz	Twisting
Third mode frequency f_3	482.21 Hz	240.35 Hz	Bending

Table 2: *Natural frequencies and modes of the plate immersed in air and in water. Table from ASME paper by Watine et al. (2020)*

The natural frequencies of the structure are associated with the highest magnitude peaks of the FRF. Table 2 presents the natural frequencies in still air and in still water of the first and second bending modes expressed as f_1 and f_3 respectively and the first twisting mode expressed as f_2. The added-mass effect is predominant as the frequency is reduced of around 50% when the plate is immersed in water. An electrical perturbation is represented by a narrow banded peak at 100 Hz. Modal shapes associated with the three first natural frequencies (f_1, f_2, f_3) are presented by figure 4.

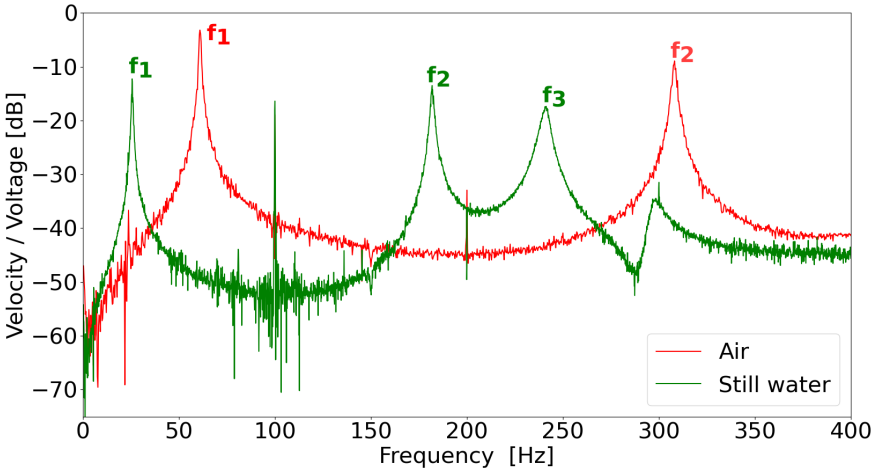

Figure 3: Vibration frequency response function of the aluminium plate at zero flow velocity with piezo excitation. Measurements are performed in air and in still water, they evidence peaks at the natural frequencies of the structure. Figure from ASME paper by Watine et al. (2020)

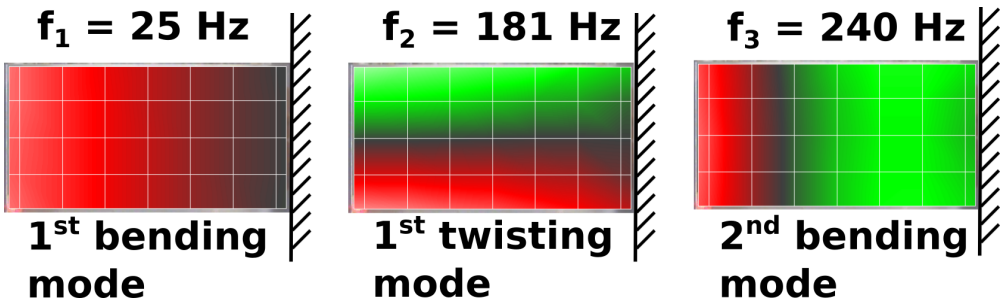

Figure 4: Modal shapes associated with the three first natural frequencies (f_1, f_2, f_3) of the structure surrounded by still water.

For the characterization of the structural vibrations induced by the fluid flow, only the spectrums recorded by the PVD-100 vibrometer at the reference point have been analysed. Table 3 resumes the specificities of

the vibration velocity spectrum computation method by welch transform. In order to evaluate the strength of the vibration at each flow regime, the root mean square velocity of each spectrum has been calculated by integration in a discrete frequency domain and is noted V_s^{rms}. In a similar way, the highest amplitude of each spectrum and it's associated frequency have also been extracted and are noted V_s^{max} and f_s^{max} respectively. Figure 5 presents an example of vibration velocity spectrum at $U_0 = 4.5\ m.s^{-1}$ and its corresponding V_s^{max} and f_s^{max}.

Time signal sampling frequency	5120 Hz
Time signal duration	80 s
Time signal average number	50
Spectrum calculation method	Welch
Number of FFT lines	2056

Table 3: Parameters used to calculate the vibration velocity spectrum of the structure under flow excitation.

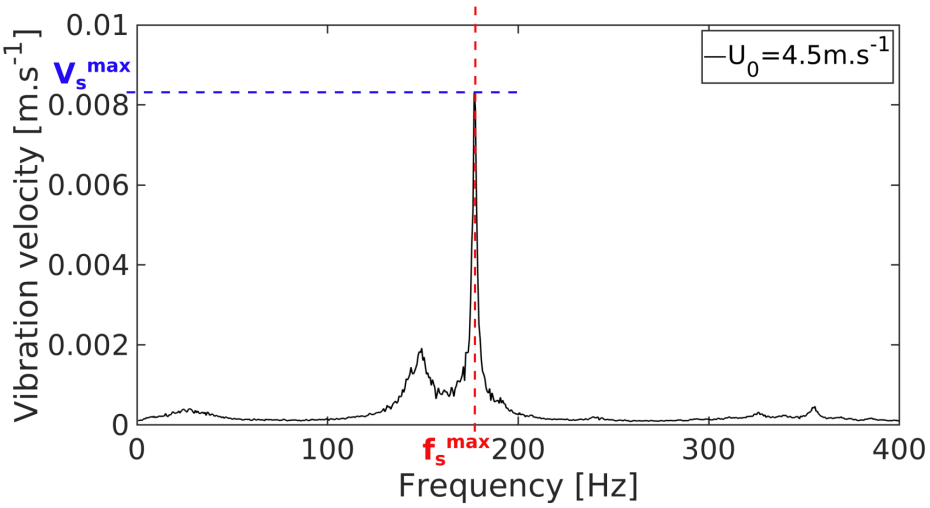

Figure 5: Vibration velocity spectrum at $Re_c = 4.5 \times 10^5$: V_s^{max} and f_s^{max} corresponds respectively to the magnitude and frequency of the highest peak.

2.4. TR-PIV

Two components time resolved particle image velocimetry (TR-PIV) has been used for the characterization of the flow downstream the plate in the symmetry plane of the tunnel (z=0). For the purpose, the flow has been seeded with polyamide particles. Time between pulses Δt_{pulse} was adjusted with respect to the upstream velocity. Table 4 summarizes the main specifications and parameters of the PIV set-up. Refer to our ASME paper by Watine et al. (2020) for additional information about the method. Exhaustive informations about the Particle Image Velocimetry technique can also be found in Raffel et al. (2007) [23].

Specifications	
Laser type	Nd:YLF
Laser wave length	527 nm
Lasers pulse duration	158 ns
Time between pulses	$\Delta t_{pulse}(\mu s) = \frac{438}{U_0(m/s)}$
Lasers pulse peak power	11.7 mJ/pulse
Sampling frequency	From 1000 to 1400 Hz, according to U_0
High speed camera type	Phantom v611
High speed camera resolution	8 bit
High speed camera lens type	Zeiss Makro Planar 100 mm
High speed camera pixel size	20 μm
Picture size	1280 × 800 pixels
Scale factor	52.5 μm/pixel
Particle type	Polyamide
Particle density	1.03 g.cm^{-3}
Particle diameter	10 ± 2 μm
Particle relaxation time	8.5 μm

Table 4: Specifications of the PIV optical device and acquisition settings.

As illustrated by figure 6, the viewing area had dimensions 67.2 × 42 mm (i.e.11.2D × 7D) in the x and y directions respectively with a scale factor of 52.5 μm/pixel. The near wake of the plate was investigated from x = −1.2 × D to x = 10 × D with a y=0 axis centred in the viewing area.

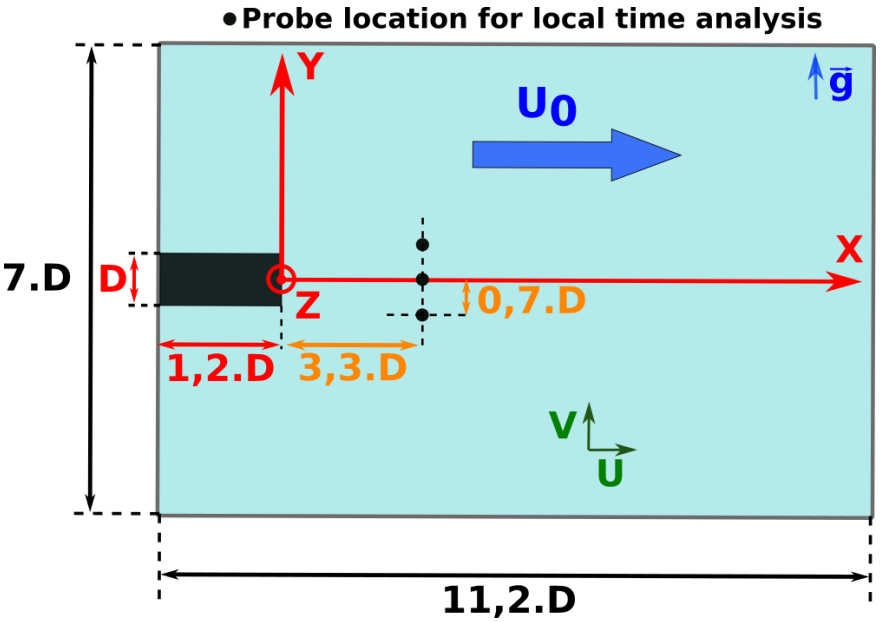

Figure 6: PIV window dimensions.

The velocity field was processed with *DynamicStudio 2015c*, using an adaptative PIV method. The square interrogation area was 16 × 16 pixels in size without overlap , which offered a spatial resolution of 0.14 × D in the x and y directions. The criteria applied for adaptative PIV processing are specified in table 5. With these criteria the validation rate was 99.9% of the measured velocity vectors. The velocity field

(u,v) was imaged at 1000 Hz and 1400 Hz (according to U_0) during a measurement time of 1 s. The analysis of the velocity field consists in different approaches: time-averaged analysis, space-time and wave-number-frequency analysis, as well as Proper Orthogonal Decomposition analysis. These different approaches will be further described in section 3.

Specifications of the PIV processing	
Interogation area size	16×16 pixels^2
No overlap	
Default validation criteria:	
- Peak height correlation	1.15
- Kernel size	5×5 pixels^2
- Universal outlier detection method	

Table 5: Specifications of the PIV processing.

2.5. Non dimensional numbers and operating points

Non dimensional numbers have been used as control parameters in order to facilitate the analysis and comparison between different velocity conditions. The main basis quantities are the free stream velocity U_0, the plate thickness D = 6 mm and chord c = 100 mm, the twisting mode natural frequency $f_2 = 180.68$ Hz, the vortex shedding frequency f_{vs} in the near wake and the kinematic viscosity $\nu = 1.10^{-6}$ m^2.s^{-1}. Accordingly, the chord based and thickness-based Reynolds numbers Re_c and Re_D and the reduced velocity RU can be expressed as:

$$Re_c = \frac{U_0.c}{\nu} \tag{1}$$

$$Re_D = \frac{U_0.D}{\nu} \tag{2}$$

$$RU_n = \frac{U_0}{f_n.D} \tag{3}$$

With f_n the n order natural frequency of the structure. The Strouhal number St_D based on the thickness has been used to characterize the flow induced vibrations. It is expressed as:

$$St_D = \frac{f_{vs}.D}{U_0} \tag{4}$$

During the lock-in with the twisting mode, the Strouhal number is equivalent to:

$$St_D = \frac{1}{RU_2} \tag{5}$$

Smaller velocity steps have been used close to the lock-in to obtain an accurate characterization of the induced phenomena.

3. Methodology and analysis techniques

The following section aims to describe the different methodologies and analysis techniques that have been applied to the (2D-2C) velocity field measured by TR-PIV.

3.1. Proper Orthogonal Decomposition

POD aims at identifying the most energetic structures in the velocity field, which can be coherent structures in a wake, and also permits the filtering of the low energy flow structures. Let $\mathbf{x}$ denote the

position vector : $\mathbf{x}$=(x,y). In the case of a statistically stationary 2D flow with a well defined time-averaged velocity field (U, V), the fluctuating velocity components are then decomposed into a sum of deterministic spatial functions $\Phi_k(\mathbf{x})$ or POD modes modulated by random time coefficients $a_k(t)$. Let us denote (Φ_k^u, Φ_k^v) the components of the eigenvector (POD modes) of mode number k. The eigenvalue λ_k is representative of the average energy captured by mode k. For a set of N fluctuating velocity fields, the expansion is truncated at order N:

$$u'(t, \overrightarrow{x}) = u(t, \overrightarrow{x}) - \bar{U}(\overrightarrow{x}) = \sum_{i=1}^{N} a_k(t)\Phi_k^u(\overrightarrow{x}) \tag{6}$$

$$v'(t, \overrightarrow{x}) = v(t, \overrightarrow{x}) - \bar{V}(\overrightarrow{x}) = \sum_{i=1}^{N} a_k(t)\Phi_k^v(\overrightarrow{x}) \tag{7}$$

In the present study the snapshot method introduced by Sirovich (1987) [24] has been applied. For additional theoretical background and mathematical demonstration in the infinite-dimensional space refer to Berkooz et al. (2003) [25], Chatterjee (2000) [26], Cordier et al. (2008) [27] and Holmes et al. (2012) [28]. The most energetic POD modes obtained in the near-wake of the plate have been analysed in details for ($1 <= k <= 10$) and compared between different conditions of the inlet velocity. An example of vorticity cartography corresponding to the 3 first POD modes is provided in Figure 7. Mode 0 represents the time-averaged vorticity. Modes 1 and 2 exhibit a symmetric distribution of the vorticity along the trailing edge centreline characterized by a streamwise periodic alternance of positive and negative vorticity. Modes 1 and 2 correspond to the Karman vortices.

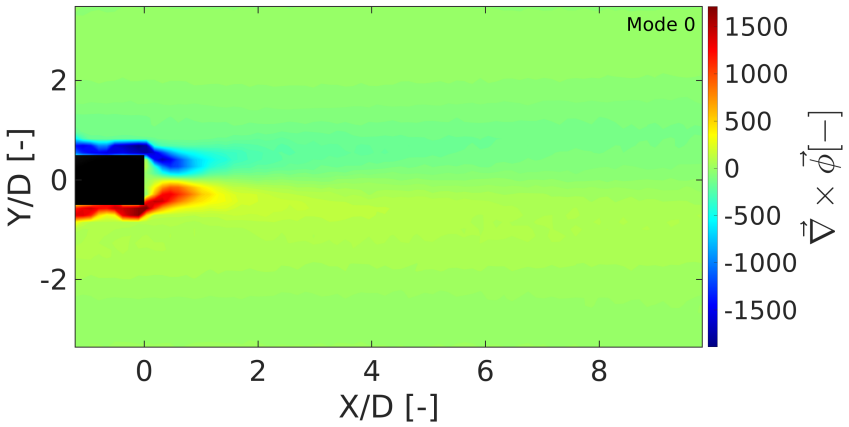

(a) Mode 0: time averaged vorticity field

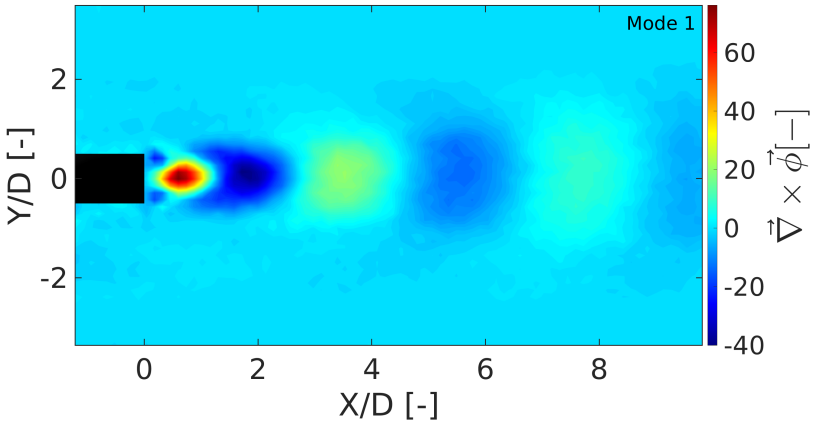

(b) Mode 1

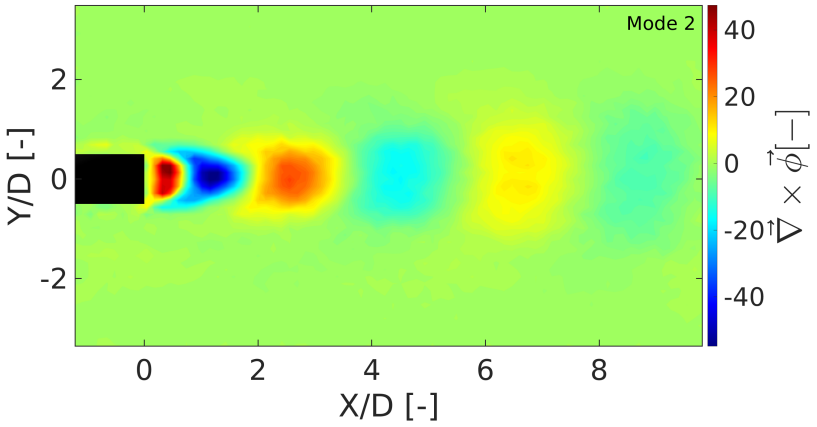

(c) Mode 2

Figure 7: (x,y) cartography of non dimensional vorticity and vector field of modes 0, 1 and 2 at $U_0 = 3.0 \text{m.s}^{-1}$. Modes 1 and 2 are characteristic of the Karman wake.

3.2. Statistical analysis

For the statistical analysis, the measured spurious velocity vectors, as well as the velocity fluctuations induced by lowest energetic turbulent structures have been suppressed from the instantaneous velocity fields by reconstruction of the velocity field as a linear combination of the modes, for which the cumulative energy is at least 90% of the total energy.

$$u_{reconstructed}(t, \overrightarrow{x}) = \bar{U}(\overrightarrow{x}) + \sum_{i=1}^{n_{90}} a_k(t)\Phi_k^u(\overrightarrow{x}) \tag{8}$$

$$v_{reconstructed}(t, \overrightarrow{x}) = \bar{V}(\overrightarrow{x}) + \sum_{i=1}^{n_{90}} a_k(t)\Phi_k^v(\overrightarrow{x}) \tag{9}$$

The local root mean square velocity components, as well as the local turbulent shear stress have been deduced from the reconstructed velocity field, as follows:

$$u_{rms}(\overrightarrow{x}) = \sqrt{\overline{u'^2_{reconstructed}}} = \sqrt{\overline{(u_{reconstructed} - \overline{U})^2}} \tag{10}$$

$$v_{rms}(\overrightarrow{x}) = \sqrt{\overline{v'^2_{reconstructed}}} = \sqrt{\overline{(v_{reconstructed} - \overline{V})^2}} \tag{11}$$

$$\overline{u'v'}(\overrightarrow{x}) = \overline{(u_{reconstructed} - \overline{U})(v_{reconstructed} - \overline{V})} \tag{12}$$

Where $\bar{}$ denotes the time average.

3.3. Time spectral analysis

The temporal evolution of the expansion coefficients $a_k(t)$ has also been analysed ($1 \leq k \leq 10$) by applying a Fast Fourier Transform algorithm . Figure 8 displays an example of frequency spectrum of the coefficient $a_1(t)$ of mode 1, characteristic of the Karman wake. The highest amplitude in the spectrum is associated to the frequency of the vortex shedding f_{vs} of the Karman vortices. Same frequency is given by mode 1 and 2, both representative of the Karman wake.

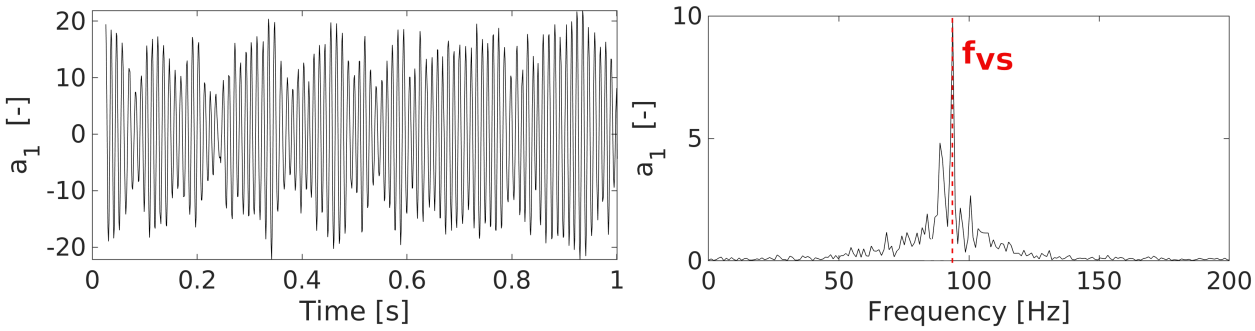

(a) (b)

Figure 8: Time evolution (a) and associated frequency spectrum (b) of the POD coefficient $a_1(t)$, characteristic of the Karman wake at $U_0 = 3.0$ m.s^{-1}. The Karman vortex shedding frequency is expressed as f_{vs} and corresponds to the highest peak of the spectrum.

3.4. Vortex detection algorithm

It is of great interest to identify the main characteristics of coherent vortices. In the present work, we have used the vortex identification and characterization methods developed by Graftieaux et al. (2001)[20]. It is based on two scalar functions, Γ_1 and Γ_2, which are derived from the 2D velocity field. These functions are able to detect the locations of the centre and the boundary of the coherent vortices, by considering only

the topology of the velocity field and not its magnitude. This method is very robust and is able to process data sets resulting from large PIV recording. The method has been applied onto the spatial mode 1 (Φ_1^u,Φ_1^v) characteristic of the Karman wake. The appendix A describes in detail the principle of the method as it has been presented by Graftiaux et al. (2001) [20].

The Γ_2 method has been used preferentially. Each vortex core is identified as an object and each vortex center has been localized as being the Γ_2 based gravity center of the vortex core. The circulation Γ of the vortex has been deduced by integrating $\overrightarrow{\nabla} \times \overrightarrow{U}$ over the vortex core area A:

$$\Gamma = \int_A \overrightarrow{\nabla} \times \overrightarrow{U} \, \mathrm{ds} \tag{13}$$

The rotation rate $\overrightarrow{\Omega}$ of the vortex is deduced from the angular momentum γ and from the inertia coefficient I averaged over the vortex core.

$$\overrightarrow{\Omega} = \frac{\overrightarrow{\gamma}}{\mathrm{I}} \tag{14}$$

with

$$\mathrm{I} = \frac{1}{\mathrm{A}} \int_A \overrightarrow{OM} \cdot \overrightarrow{OM} \, \mathrm{ds} \tag{15}$$

and

$$\gamma = \frac{1}{A} \int_A \overrightarrow{OM} \wedge \overrightarrow{U_M} \, ds \tag{16}$$

Figure 9 displays an example of spatial mode 1 with the identified vortices cores superimposed.

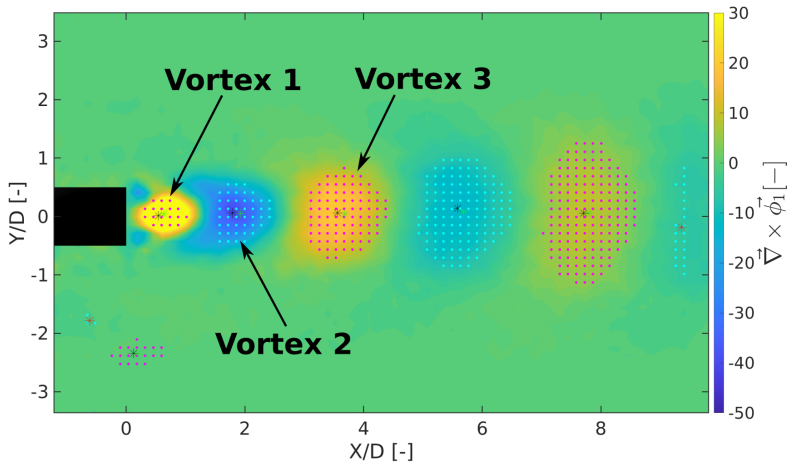

Figure 9: Example of vortex detection applied at $U_0 = 3.0$ m.s^{-1} mean flow velocity on spatial mode 1. Blue dots represent the detection of the negative rotation rate vortices, magenta dots the positive rotation rate vortices with the Γ_2 method. The vortex centres have been detected with the Γ_1 (black star) and Γ_2 methods (green star). The Γ_2 method is preferred because the detection of the vortex centres is more in accordance with the morphology of the vortical structures. Vortices detected outside of the near wake region have not being taken into account.

4. Vibrations of the structure under flow excitation

The fluid structure interaction process has been identified as a vibratory response of the structure to an hydrodynamic excitation source consisting mainly in vortex shedding at the trailing edge of the plate. The

following sections aims to analyse the evolution with the Reynolds number of the vortex shedding frequency of the Karman wake together with the vibration specificities of the structure. This analysis makes it possible to identify some particular vibratory regimes. A constant Strouhal number implies a linear evolution of the vortex shedding frequency f_{vs} with the free stream velocity U_0 and is proper to non resonant regimes.

Figure 10 presents, at various Reynolds, the vortex shedding frequency f_{vs} and the dominant frequency f_s^{max}. Linear scaling of the vortex shedding frequency are visible for Reynolds Re_c ranging in $[2.5 \times 10^5 - 5.1 \times 10^5]$ and $[6.0 \times 10^5 - 9.5 \times 10^5]$. A constant Strouhal number $St_D = 0.189 \pm 0.003$ has been reported for these Reynolds ranges. Data about the Strouhal number are missing in the survey for large chord to thickness ratios and high Reynolds numbers. For $c/D > 12$ and $Re_D > 2 \times 10^3$, Nakamura et al. (1991) [7] did not observe an organised vortex shedding with a characteristic peak frequency. This disorganisation of the vortex street was confirmed by Parker et al. (1983) [4] in the range $[1.4 \times 10^4 - 3.1 \times 10^4]$. However, for larger c/D values ($c/D > 16$), the vortex shedding becomes more regular again and is characterized by a broadband peak in the velocity spectra. In this case, for large c/D values and Re_D in the range $[1.4 \times 10^4 - 3.1 \times 10^4]$ corresponding to a reorganized vortex shedding, the Stouhal number of the blunt plate approximates the values of plates with a similar geometry and rounded leading edges (Parker et al. (1983) [4]). The value $St_D = 0.195$ of our experiments is consistent with the value $St_D = 0.20$ measured for a flat plate with rounded edges of same c/D, Blevins (1977) [29]. Note that $St_D = 0.195$ is the Strouhal number observed in the wake of cylinders for turbulent shedding conditions and Re_D in the range $[1.0 \times 10^4 - 2.0 \times 10^4]$, Norberg (2001) [30].

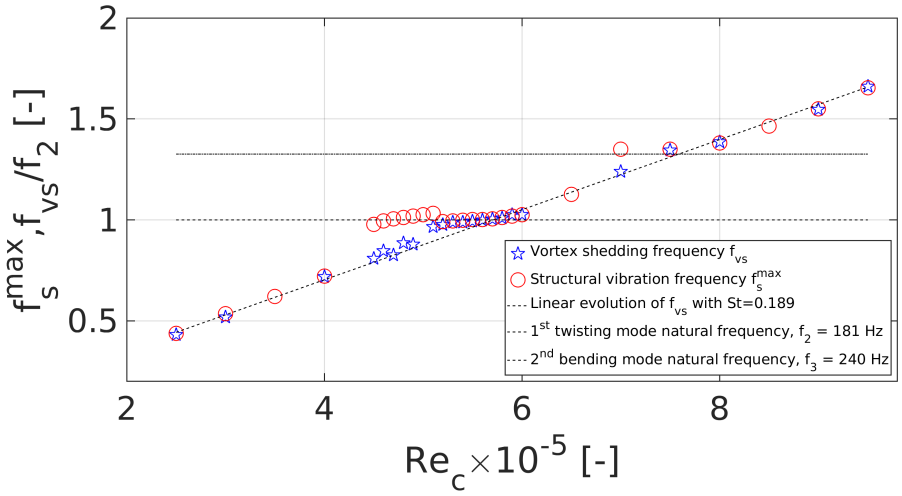

Figure 10: Evolution with Reynolds of the structural vibration frequency f_s^{max} and Karman vortex shedding frequency f_{vs} scaled by f_2. Maximal uncertainty is 0.6 Hz for f_s^{max} and 1 Hz for f_{vs}.

The frequency-Reynolds diagram presented by Figure 11 highlights some linear evolution of f_s^{max} with Re_c in the intervals $[2.5 \times 10^5 - 4.0 \times 10^5]$ and $[6.0 \times 10^5 - 6.5 \times 10^5]$ and $[8.0 \times 10^5 - 9.5 \times 10^5]$. The linear evolution of f_s^{max} is characteristic of non resonance regimes where f_s^{max} is driven by f_{vs} as a consequence of vortex shedding induced vibrations.

Lock-in occurs when an excitation frequency is equal to a natural frequency of the system. It has been observed that in this situation the structural vibration dominant frequency f_s^{max} is equal to the twisting mode natural frequency f_2 and to the vortex shedding frequency f_{vs}. According to figures 10 and 11 this happens for Reynolds included in $[5.2 \times 10^5 - 6.0 \times 10^5]$ for lock-in with the twisting mode (f_2) and for Reynolds included in $[7.5 \times 10^5 - 8.0 \times 10^5]$ for lock-in with the bending mode (f_3). As can be seen on figure 11, the vibration spectra are fulfilled at high frequencies in the lock-in regimes and exhibit high vibration amplitude peaks at harmonics of the natural frequency of the structure. A somewhat particular resonance

regime has been observed for Reynolds included in $[4.5 \times 10^5 - 5.1 \times 10^5]$. This regime, named here lock-off resonance, is characterized by a dominant structural vibration frequency f_s^{max} equal to the twisting mode natural frequency f_2 but different from the vortex shedding frequency f_{vs}. A similar trend has been observed during the resonance with the second bending mode (f_3) for Re_c included in $[7.0 \times 10^5 - 7.5 \times 10^5]$. However, the number of measurement points is to small for this last range of Reynolds number to assume precise characterization of the bending lock-off resonant regime. The observation of the lock-off resonance may be of great interest for designers as it introduces the fact that high amplitude vibrations may occur for Reynolds numbers lower than those expected at the lock-in.

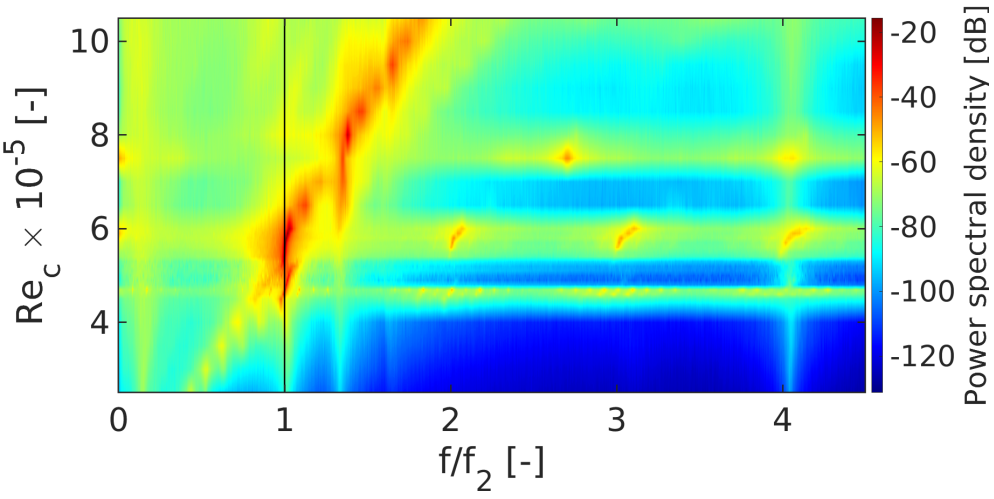

Figure 11: Cartography of the power spectral density of the structure vibration velocity. Cartography in the plane (f_s/f_2, Re_c). Power spectral density expressed in dB ($Vs_{ref} = 1$ m.s^{-1}). Figure extracted from our ASME paper, Watine et al. (2020) [21].

Complementary to the vibration frequency and Karman vortex shedding frequency evolutions with Reynolds, the magnitude of the vibrating velocity has been evaluated. For the purpose, both quantities, V_s^{rms} and V_s^{max}, normalized by f_2D, are plotted in figure 12 with regard to Re_c. It reveals that the highest vibration magnitude appears during the lock-in regime with an overall maximum at Reynolds equal to 5.7×10^5 ($RU_2 = U_0/f_2D = 5.25$) corresponding to the first twisting mode lock-in at f_2. A second maximum is visible at Reynolds equal to 8.0×10^5 ($RU_3 = U_0/f_3D = 5.56$) and corresponds to the lock-in with the second bending mode (f_3). At lock-in with f_2, $St_D = 1/RU_2 = 0.19$ which is in agreement with the Strouhal value.

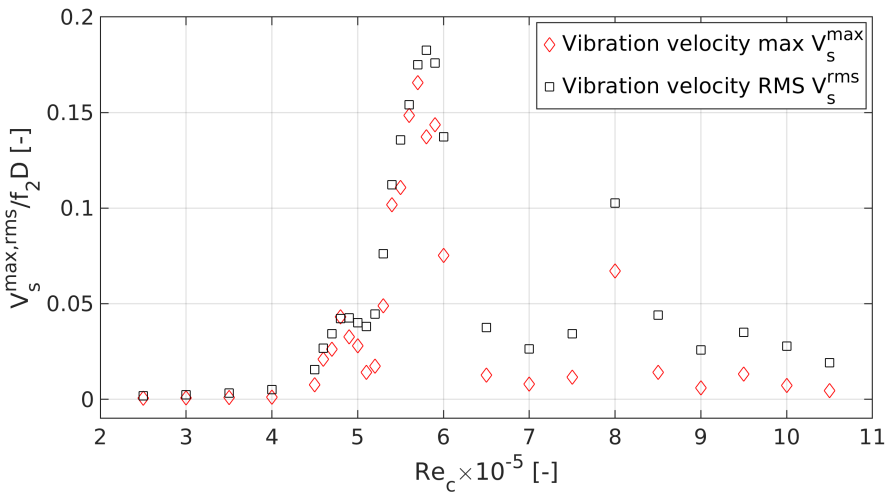

Figure 12: Evolution of V_s^{rms} and V_s^{max} with Reynolds. Maximal uncertainty on V_s^{rms} is $\pm 2.17 \times 10^{-4}$ m.s^{-1}.

This observation is in accordance with the results of Ausoni (2009) [19] claiming that an hydro-elastic coupling appears for flow velocities close to the ones of the lock-in regime, even if the structure oscillates at its natural frequency, the magnitudes of vibrations are not high enough to impose the natural frequency of the structure to the wake. This may explain why the vortex shedding frequency f_{vs} is still different from the eigenfrequency f_2 for the lock-off resonance regime. For this regime, a local maximum of vibration velocity amplitude is observed at Re_c equal to 4.8×10^5. It should also be noticed that the vibration intensity remains almost constant beside the resonance regimes even if the Reynolds number increases. Observations made previously, have permitted to define different regimes of fluid-structure interaction which are summarized in table 6 depending on a specific Reynols number range or reduced velocity range. Based on these identified regimes, 3 operating points have been selected (A, B, C). Each of them corresponds to a particular regime with regard to the twisting resonance mode. Point A corresponds to no resonance, point B to resonance without lock-in (lock-off resonance) and point C to the lock-in. Points B and C are conditions of local maxima of V_s^{rms}. The characteristics of these operating points are summarized in table 7.

Reynolds range	**RU range**	**Regime**	**Frequencies**
$2.5 \times 10^5 \leq Re_c \leq 4.5 \times 10^5$ $1.5 \times 10^4 \leq Re_D \leq 2.7 \times 10^4$	$2.30 \leq RU_2 \leq 4.14$	No resonance	$f_{vs} = f_s^{max} \neq f_2$
$4.5 \times 10^5 \leq Re_c \leq 5.1 \times 10^5$ $2.7 \times 10^4 \leq Re_D \leq 3.1 \times 10^4$	$4.14 \leq RU_2 \leq 4.70$	Resonance No lock-in	$f_{vs} \neq f_s^{max} = f_2$
$5.1 \times 10^5 \leq Re_c \leq 6.0 \times 10^5$ $3.1 \times 10^4 \leq Re_D \leq 3.6 \times 10^4$	$4.70 \leq RU_2 \leq 5.53$	Resonance and lock-in	$f_{vs} = f_s^{max} = f_2$
$6.0 \times 10^5 \leq Re_c \leq 7.0 \times 10^5$ $3.6 \times 10^4 \leq Re_D \leq 4.2 \times 10^4$	$4.17 \leq RU_3 \leq 4.86$	No resonance	$f_{vs} = f_s^{max} \neq f_3$
$7.0 \times 10^5 \leq Re_c \leq 7.5 \times 10^5$ $4.2 \times 10^4 \leq Re_D \leq 4.5 \times 10^4$	$4.86 \leq RU_3 \leq 5.21$	Resonance No lock-in	$f_{vs} \neq f_s^{max} = f_3$
$7.5 \times 10^5 \leq Re_c \leq 8.0 \times 10^5$ $4.5 \times 10^4 \leq Re_D \leq 4.8 \times 10^4$	$5.21 \leq RU_3 \leq 5.56$	Resonance and lock-in	$f_{vs} = f_s^{max} = f_3$
$8.0 \times 10^5 \leq Re_c \leq 9.5 \times 10^5$ $4.8 \times 10^4 \leq Re_D \leq 5.7 \times 10^4$	$5.56 \leq RU_3 \leq 6.60$	No resonance	$f_{vs} = f_s^{max} \neq f_3$

Table 6: Summary of the different fluid structure interaction regimes according to Re_c range, Re_D range and RU range.

	Reynolds	RU_2	**Regime**	**Frequencies**	Local max of V_s^{rms}
(A)	$Re_c = 3.0 \times 10^5$ $Re_D = 1.80 \times 10^4$	2.76	No resonance	$f_{vs} = f_s^{max} \neq f_2$	No
(B)	$Re_c = 4.8 \times 10^5$ $Re_D = 2.88 \times 10^4$	4.42	Lock-off, resonance	$f_{vs} \neq f_s^{max} = f_2$	Yes
(C)	$Re_c = 5.7 \times 10^5$ $Re_D = 3.42 \times 10^4$	5.25	Lock-in	$f_{vs} = f_s^{max} = f_2$	Yes

Table 7: Points of interest and associated vibration regimes and characteristics.

The general features of the vibrational response of the plate have been investigated in order to understand the fluid structure interaction process responsible of high magnitudes vibrations. Attention will now be paid to the hydrodynamic properties of the flow downstream the plate. In a first instance the general features of the near-wake will be studied.

5. General features of the near-wake

The analysis of the statistical quantities based on the computation of the time averaged velocity fields enables to study the general specificities of the near-wake.

5.1. General remarks

The time averaged velocity fields of the U and V velocity components are presented by figures 13a and 13b respectively at a chord based Reynolds number Re_c equal to 3.0×10^5 corresponding to point A (a low amplitude vibration regime out of resonance). The wake region is characterized by a substantial decrease of the streamwise mean velocity component U. A strong gradient in the velocity profiles $\frac{\partial U}{\partial X}$ is visible for X/D

included in [0-4] which is characteristic of the very near wake. Two regions of high magnitude of vertical mean velocity components V are visible for X/D included in [0 - 2] with a maximum of $|V|/U_0 \simeq 0.2$ at $X/D = 0.7$.

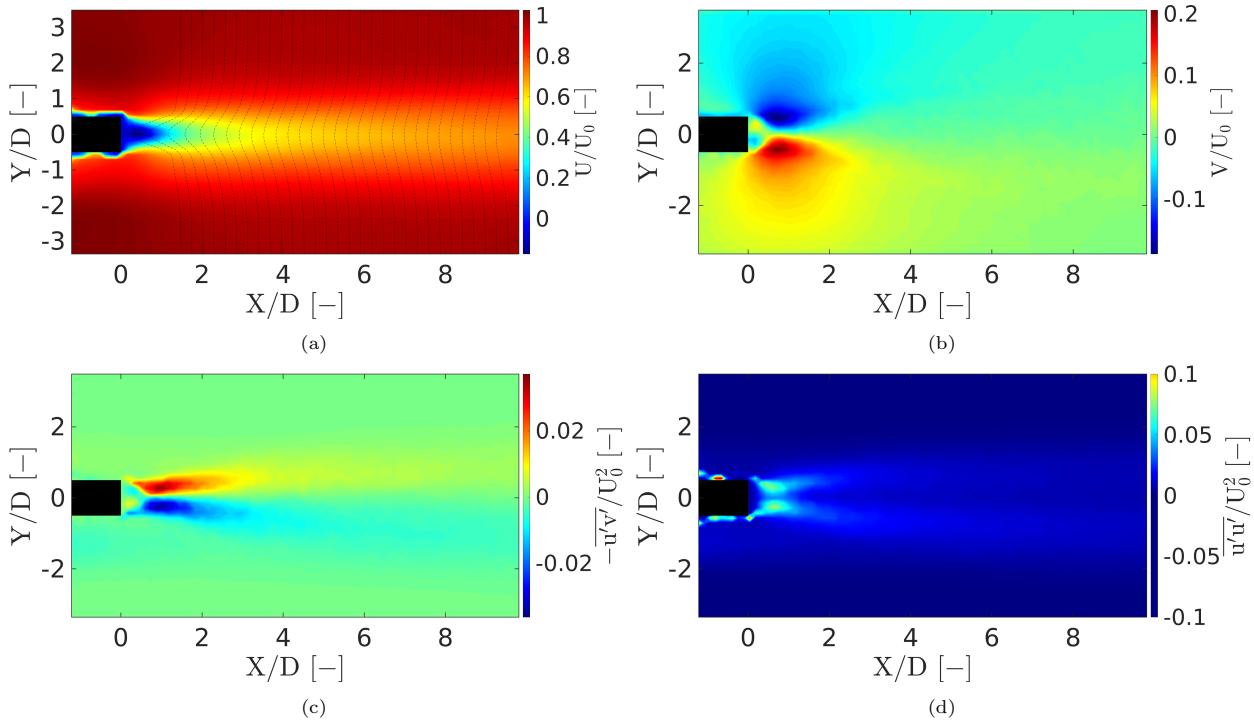

Figure 13: (x,y) cartography of the time averaged horizontal (a) and vertical (b) velocity components U and V, the Reynolds shear stress $-\overline{u'v'}/U_0^2$ (c) and the Reynolds normal streamwise stress $\overline{u'u'}/U_0^2$ (d) at $U_0 = 3.0$ m.s^{-1}. Cartographies based on the reconstructed velocity field.

This induces a recirculation region composed of two counter rotating vortices for X/D included in $[0-1]$ and Y/D in $[-0.5; 0.5]$. In the paper, we will also refer to the term wake bubble (WB) to name the recirculation region. This recirculation region is highlighted when plotting the streamlines, as presented in figure 14. This particular region is characterized by negative magnitudes of the horizontal velocity component U which induces a reversed flow. The reversed flow ends at the reattachment point of the wake at $X = L_R \simeq D$. This value is in agreement with the value measured by Taylor et al. (2011) [31] for $Re_c = 2.1 \times 10^5$ and $c/D = 7$.

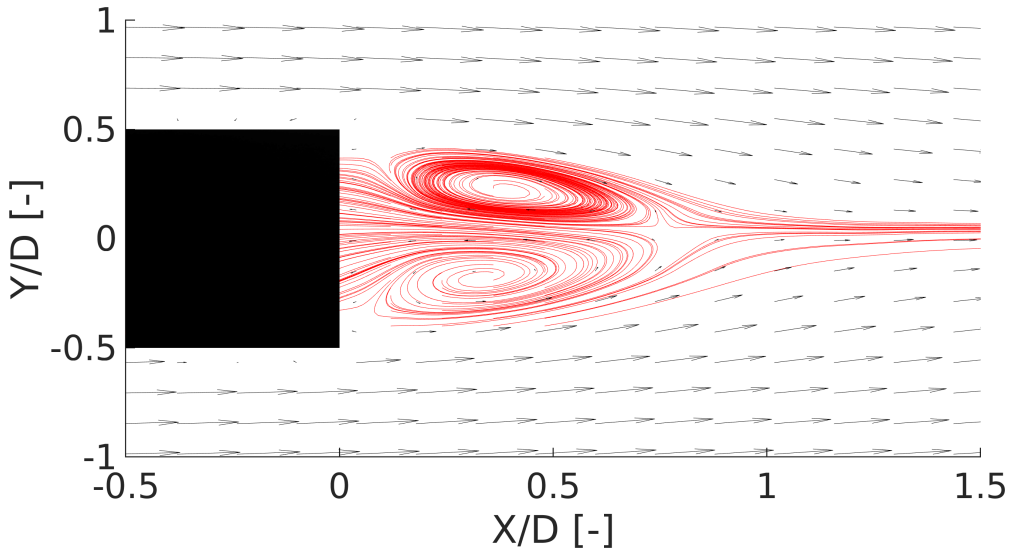

Figure 14: Streamline pattern superposed to the time averaged (x,y) velocity field at $U_0 = 3.0$ m.s^{-1}. For clarity purpose the streamlines under and above the plate have been hidden.

Figure 13c presents a (x,y) cartography of the Reynolds shear stress $-\overline{u'v'}/U_0^2$. High magnitude positive and negative shear stress regions are visible for X/D included in $[0-4]$. These regions of high $|u'v'|$ delineate the recirculation area. Also, one can observe a region of zero Reynolds stress inside the recirculation area on both sides of the wake centreline. This particular region is expected to be the region where minimum pressure occurs, as discussed by Taylor et al. (2011) [31]. The patterns of shear stress observed are in agreement with earlier studies and highlight the assertion of Balachandar et al. (1997) [32] stating that the pattern of the shear stress regions is a consequence of the vortex shedding activity over a cycle. Figure 13d shows a (x,y) cartography of the normal Reynolds stress in the streamwise direction $\overline{u'u'}/U_0^2$. The highest amplitude of this Reynolds stress can delineate the recirculation region.

5.2. Evolution with Reynolds of the time averaged characteristics of the recirculation region

The following paragraphs aims to describe the evolution with Reynolds of some general properties of the near wake region such as the vortex formation length, as well as the maxima of Reynolds shear stress and the streamwise velocity deficit.

Chopra et al. (2019) [33] defines the vortex formation length L_e as the distance over which the vortices shed in the near wake achieve their maximum strength while they convect. A common method to asses L_e consists in evaluating the streamwise distance between the trailing edge and the point along the wake axis where the time averaged Reynolds stress $\overline{u'u'}$ is maximum, Bearman (1965) [34], Griffin (1995) [35], Kovasnay et al. (1949) [36]. Complementary to this definition we have investigated the location along the wake axis where the time averaged shear stress $-\overline{u'v'}$ reaches its maximum absolute value (maximum of $|\overline{u'v'}|$) for Y<0 and Y>0. These quantities have been assessed for various chord based Reynolds numbers in order to analyse the evolution of the vortex formation length as the inflow velocity U_0 increases.

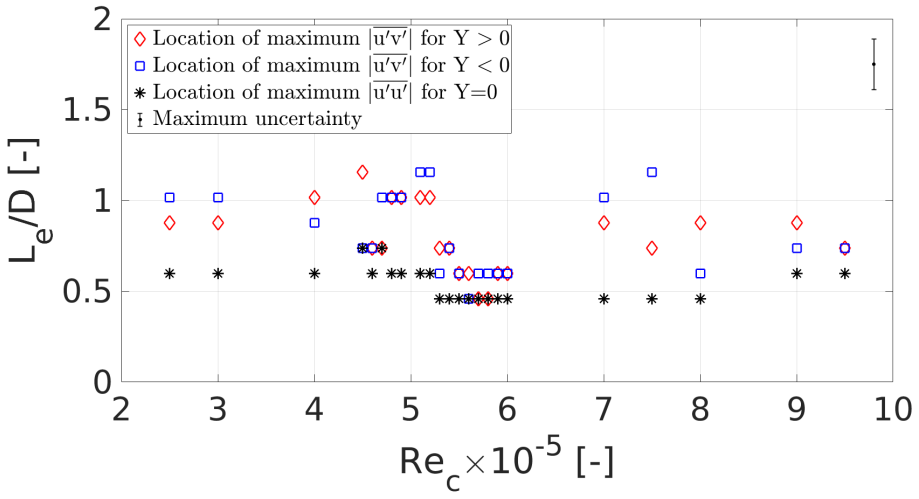

Figure 15: Evolution of the vortex formation length L_e with Re_c

As presented by figure 15 the vortex formation length using the location of maximum $\overline{u'u'}$ varies between 0.45 and 0.75, but regarding the spatial resolution of the PIV vector fields it is hazardous to extract some general conclusions. Nevertheless the tendency seems to be that the vortex formation length remains mostly constant as Re_c increases in the measurement range. Regarding the evolution of the location of the maximums of $\overline{u'v'}$, a decrease of L_e is visible for Re_c ranging between 5.4×10^5 and 6.0×10^5. This corresponds to inflow velocities in the lock-in regime which means that the length of the recirculation region is reduced at lock-in with the twisting mode. In general, a shorter vortex formation length is associated to a decrease in pressure at the base of the trailing edge, Williamson et al. (2008) [37]. Indeed the minimum of pressure is shiffted closer to the trailing edge, thus leading to an increase in the pressure drag.

The peak values of the turbulent shear stress $\overline{u'v'}$ have been investigated for various Reynolds numbers as is presented by figure 16. Interestingly, maxima of $|-\overline{u'v'}/U_0^2|$ seems to be almost constant regardless of the Reynolds number, except at the lock-in with the twisting mode. A steep increase happens for Reynolds ranging between 5.1×10^5 and 6.0×10^5 with a maximum reached at 5.7×10^5. This Reynolds range corresponds to the highest vibration amplitudes occurring at the lock-in with the twisting mode which means that the recirculation is enhanced inside the recirculating region. The changes observed at lock-in: reinforcement of the recirculation and decrease of the eddy formation length play in favour of an increase in the minimum pressure and pressure drag at lock-in.

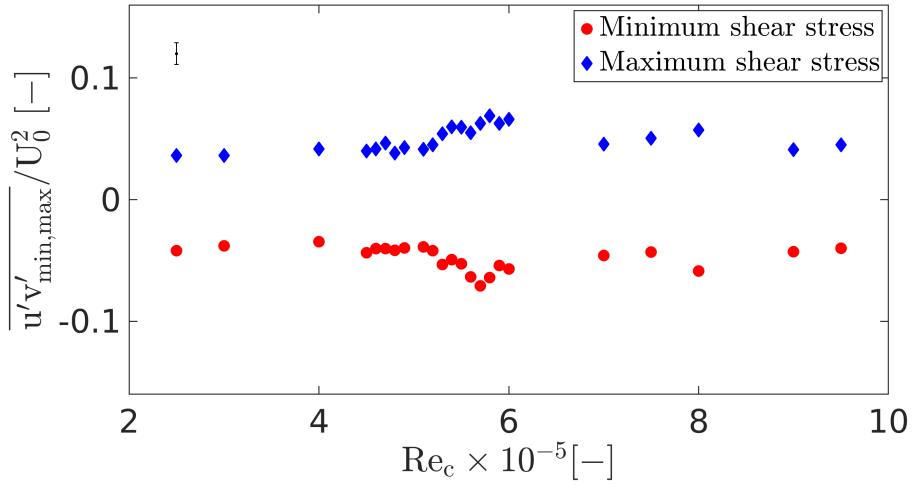

Figure 16: Evolution of min and max of u'v' with Re_c.

5.3. Time averaged velocity defect in the wake according to the vibration regime

The vertical profiles of the normalized velocity deficit $\frac{U_{defect}}{U_0} = \frac{U_0-U}{U_0} = f(\frac{Y}{D})$ measured at X=4D are displayed by figure 17 for Re_c of the points of interest. According to the theory of self-similarity of the fully turbulent plane wake, in the far field, the velocity defect measured at the centreline $\frac{U_{defect}}{U_0}$ is scalled with $\sqrt{\frac{C_D.c}{x}}$. At fixed X positions, comparison of this velocity defect makes it possible to conclude about the drag coefficient C_D. The drag coefficient obviously decreases with increasing Re_c numbers, except at the lock-in with the twisting mode ($Re_c = 5.7 \times 10^5$), which is also in agreement with a reinforcement of the recirculating region.

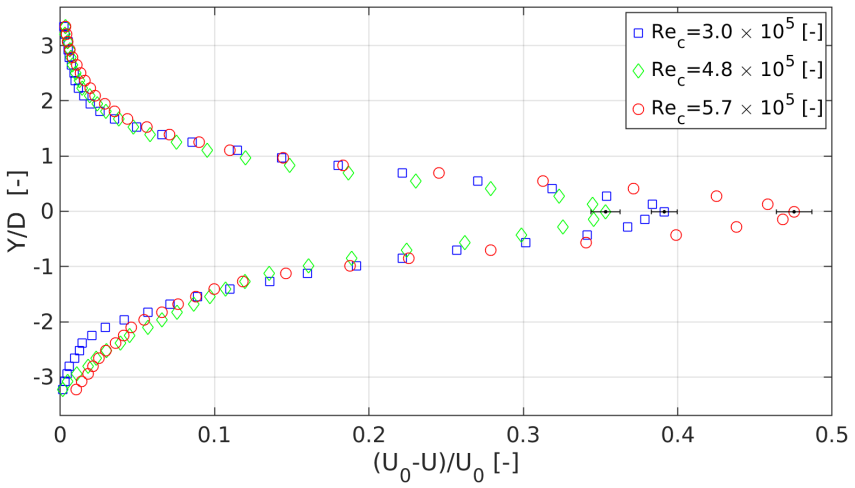

Figure 17: Vertical profiles of the normalized velocity defect $\frac{U_0-U}{U_0} = f(\frac{Y}{D})$ measured in the streamwise direction at X=4D at various Re_c numbers.

The next part of our analysis will focus on the Karman vortices which are the predominant coherent structures in the near wake. The influence of Re_c on the Karman vortices main specificities will be

investigated.

6. Influence of the Re number and the vibration regimes on the Karman vortices properties

As has been demonstrated before, the POD method offers a classification of wake structures depending on their turbulent kinetic energy (TKE) level. As a consequence the first modes contain the highest percentage of kinetic energy. For all $\mathrm{Re_c}$ numbers the two first high TKE modes are identified as Karman modes and present high spatial coherence, see figure 7. They are characterised by high alternating vorticity regions that are advected behind the trailing edge. Analysis of these structures is of great interest as they play an important part in the flow induced vibration mechanism. The present section aims to describe the evolution of the main characteristics of the Karman vortices with the Reynolds number. In particular, we focus on their contribution to the total kinetic energy, their advective velocity, streamwise wavelength and their size, rotation rate and circulation, according to the Reynolds number and vibration regime.

6.1. Karman modes total energy

The evolution of the Karman wake energy with Reynolds offers a first insight into the contribution of the Karman wake at the various various regimes. As presented by figure 18, modes 1 and 2 are characterized by similar contributions to the total energy and follow the same trend as Reynolds increases. Accordingly, the sum of the energy of modes 1 and 2 provides the total turbulent kinetic energy associated with the Karman wake. Generally speaking, the part of the total TKE contained in modes 1 and 2 decreases with increasing Reynolds number, which is in agreement with an increasing contribution to the total TKE of smaller structures, with increasing Re_c. This trend is observed in the regime out of resonance of the plate. As expected the Karman modes reach the highest energy level at the lock-in regimes occurring at 5.7×10^5 for the synchronization with the first twisting mode ($\mathrm{f_2}$) and at 8.0×10^5 for the synchronization with the second bending mode ($\mathrm{f_3}$). A local maximum occurs at the lock-off resonance regime (4.8×10^5) which is in accordance with the local maximum of vibration velocity magnitude observed at this regime. This behaviour is very similar to the results of Ausoni (2009) [19], and is identified as a hydro-elastic coupling.

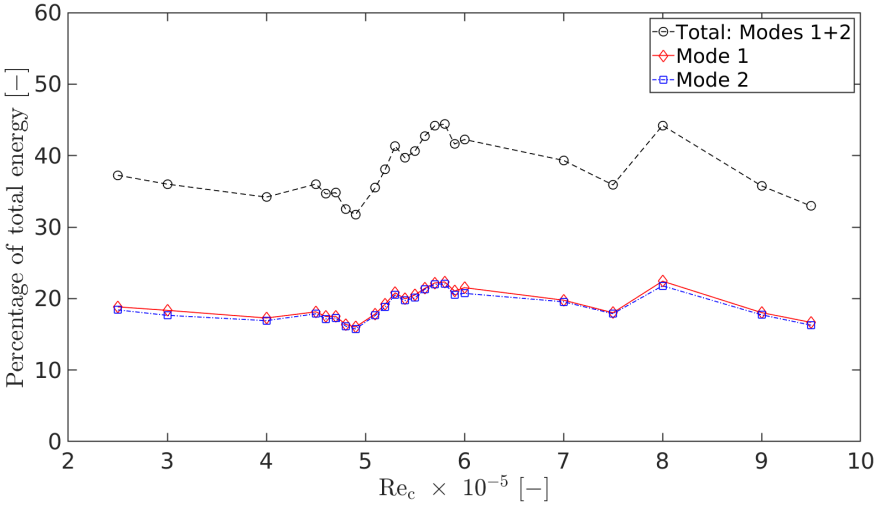

Figure 18: Mode 1 and 2 cumulated energy as a percentage of the total turbulent kinetic energy.

6.2. Advection of the Karman vortices

Figure 20 displays a zoom of the space-time diagram of the vertical velocity component $v_{1,2}$ associated to the contribution of POD modes 1 and 2:

$$v_{1,2} = a_1(t)\Phi_1^v + a_2(t)\Phi_2^v \tag{17}$$

The alternance of maxima of positive and negative $v_{1,2}$ values, which is representative of vortices, is propagating in the X downstream direction when combining modes 1 and 2. The associated wave length λ_{vs} as well as the frequency f_{vs} of the Karman shedding vortices is obtained with a 2D spectrum. A constant value of $\lambda_{vs} = 3.7D \pm 1.9D$ has been observed for the whole Reynolds range including all vibration regimes. f_{vs} is in agreement with f_{vs} determined from the FFT spectra of $a_1(t)$. The phase velocity can be deduced from $U_\Phi = \lambda_{vs} f_{vs}$. Figure 19 presents the phase velocity at various Re_c. For the regime out of resonance, we obtain $U_\Phi/U_0 \approx 0.7 \pm 0.05$. This value is larger than the value measured by Taylor et al. (2011) [31] for a blunt plate of $c/D = 7$ which was $U_\Phi/U_0 = 0.5$ for $St_D = 0.15$ at $Re_D = 3.0 \times 10^4$ but as was demonstrate by Taylor et al. (2011) for different edge geometries a larger U_Φ/U_0 value is in agreement with a larger vortex shedding frequency (i.e larger Strouhal). Indeed, Taylor et al. (2011) experienced the same value $U_\Phi/U_0 = 0.7$ for a Strouhal number of 0.19 as in our experiment but it was obtained for triangular edges. A slight increase of the phase velocity has been observed at $Re_c = 5.1 \times 10^5$ in the lock-off resonance regime with the twisting mode. For this Reynolds number, $U_\Phi/U_0 = 0.75$.

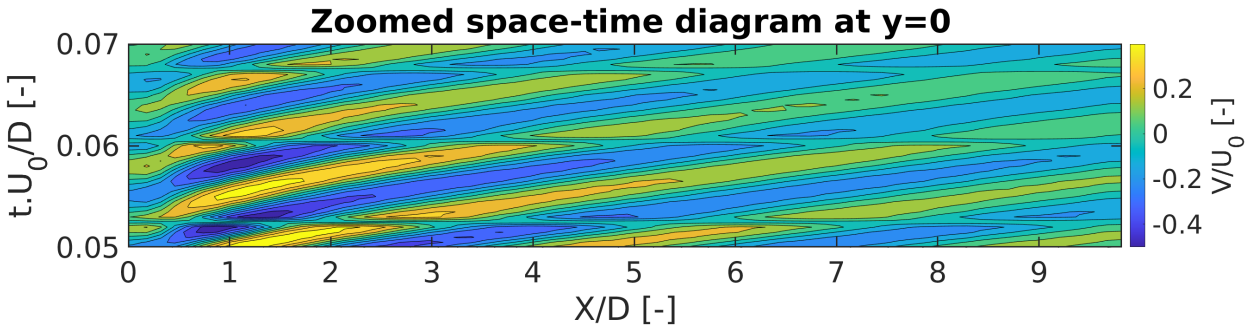

Figure 19: Space time diagram of the Karman wake (modes 1 and 2 combined) at $Re_c = 3 \times 10^5$

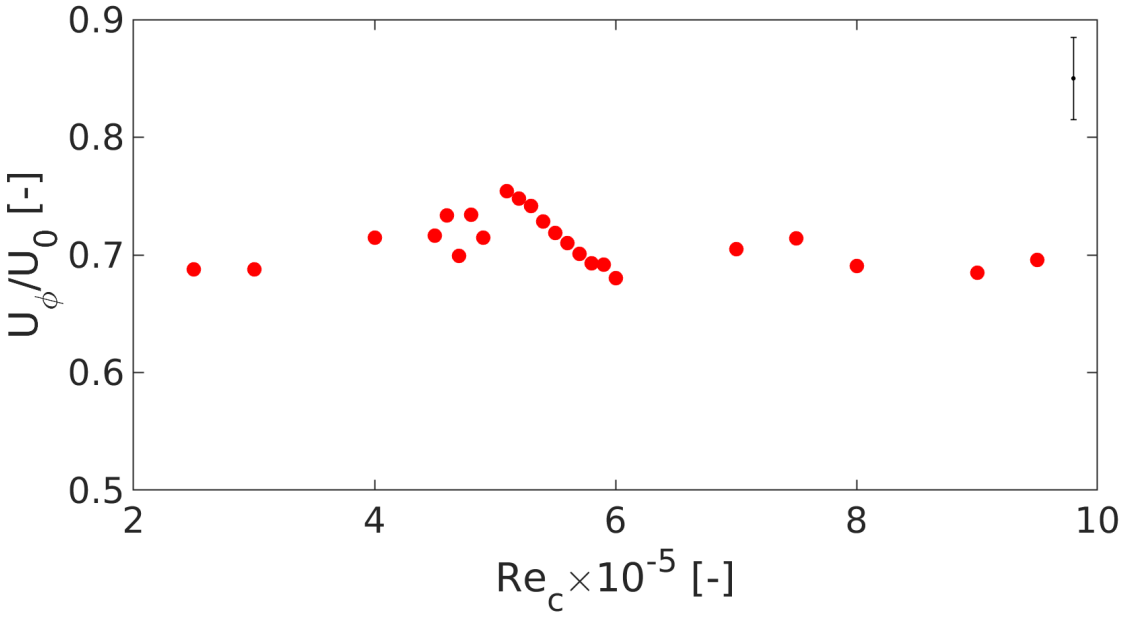

Figure 20: Evolution of the phase velocity obtained by spatio-time analysis of the reconstructed karman wake (modes 1 and 2).

6.3. Coherence of the Karman modes

As inspired from the work of Oudheusden et al. (2005) [38], the phase plot of POD coefficients $a_1(t)$ and $a_2(t)$ is useful for the analysis. This representation highlights the fact that $a_1(t)$ and $a_2(t)$ are not independent but are phase correlated. As presented by figure 21 the phase plot is modelled by a circle for ideal two-dimensional vortex shedding. Scattering from the circle can come from small scale fluctuations due to turbulence, as well as from possible inconsistent vortex shedding. Figure 21 evidences the highest coherence during the lock-in regime. The lowest coherence was observed during the lock-off resonance regime. As will be described further this is due to intermitency of the Karman vortex shedding due to the coexistence of two different characteristic frequencies in the Karman wake (f_{vs} and f_2) at this regime.

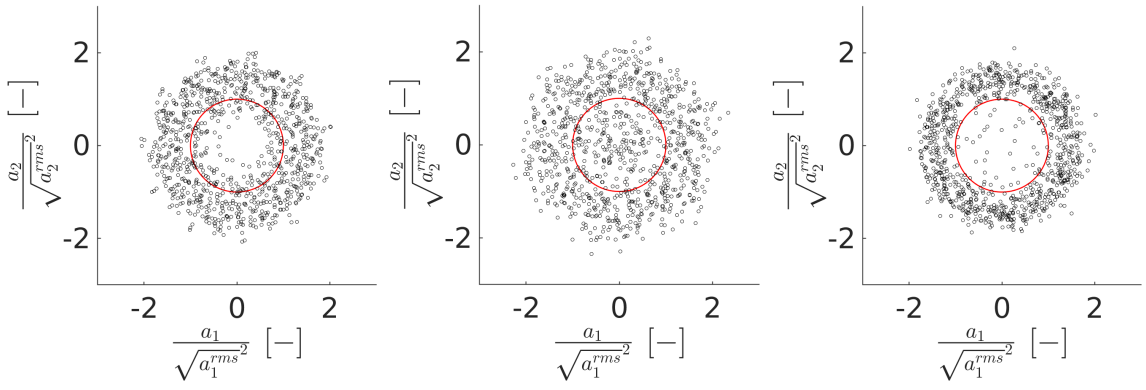

(a) $Re_c = 3.0 \times 10^5$ (b) $Re_c = 4.8 \times 10^5$ (c) $Re_c = 5.7 \times 10^5$

Figure 21: Phase diagram associated with modes 1 and 2 at the Reynolds numbers of interest. The red circle has a radius equal to 1.

6.4. Vortex core properties

As modes 1 and 2 present similar spatial coherence, the Γ_2 vortex core detection algorithm has only been applied to mode number 1 in order to reduce computation cost. The detection will consider the first, second and third vortices arranged in the streamwise (see figure 9 for a visual inspection of vortices 1, 2 and 3 cores). Of great interest is also the evolution of the vortex features as the distance from the trailing edge increases. Vortex features of interest are the vortex area A, the vortex circulation Γ and the vortex rotation rate Ω. The definition of each of these quantities is given in part 3.4. Note that in the following, the rms values of the vortex characteristics (rotation rate Ω_{rms} as well as the circulation Γ_{rms}, are determined using the rms values of the expansion coefficients of mode 1 velocity field integrated over the vortices core:

$$\mathrm{u}_{\mathrm{rms}}(\overrightarrow{x}) = \mathrm{a}_1^{\mathrm{rms}}\phi_1^{\mathrm{u}}(\overrightarrow{x}) \tag{18}$$

$$\mathrm{v}_{\mathrm{rms}}(\overrightarrow{x}) = \mathrm{a}_1^{\mathrm{rms}}\phi_1^{\mathrm{v}}(\overrightarrow{x}) \tag{19}$$

6.4.1. Vortex area

The variation of the vortex area of the three first vortices behind the trailing edge has been evaluated at various Reynolds numbers for mode number 1. It has been made dimensionless by division with the squared thickness. According to figure 22 it has been observed obviously that the vortices grow when the distance from the trailing edge increases in agreement with downstream expansion of the wake. The highest vortex area has been detected for Reynolds ranging between 5.6×10^5 and 6.0×10^5. This Reynolds range corresponds to the flow velocities where the lock-in phenomenon occurs and where the maximum vibration amplitudes is reached. Accordingly it can be affirmed that the lock-in with the twisting mode is characterized by a sudden increase of the vortex area which is in agreement with the increase of the drag pressure. A slight noticeable increase of the vortex area is also observed at the lock-in with the second bending mode ($\mathrm{Re_c} = 8 \times 10^5$). For Reynolds numbers out of the lock-in regimes, the vortex area of the vortex downstream (vortex 3) obviously decreases with increasing Reynolds number. For this regime, this obeys to a decrease with Re_c of the wake thickness (in the far wake) as a consequence of a decrease with Re_c number of the drag coefficient.

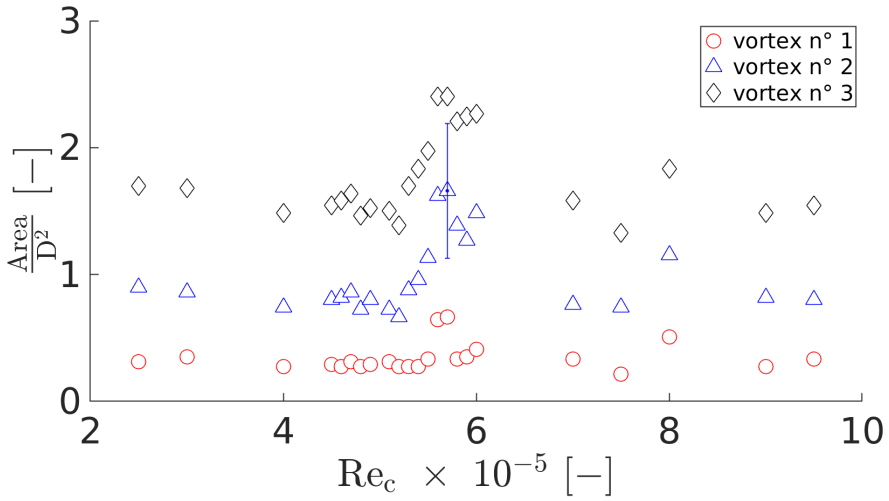

Figure 22: Non dimensional vortex core area evolution with the Reynolds number of the three first vortices downstream of the trailing edge (mode1). Vortex 1 is the upstream vortex and vortex 3 is the downstream vortex. Maximum uncertainty induced by the vortex core detection method is achieved at Re_c of the lock-in. The cores ponding error bars are plotted for the 3 vortices.

All the characteristics of vortex 2 measured for $Re_c = 4.8 \times 10^5$ (i.e $Re_D = 2.88 \times 10^4$) can be compared to characteristics of the vortices measured at $X/D = 2$ by Taylor et al. (2011) [31] at the same Re_D number for a plate of aspect ratio $c/D = 7$ with triangular edges giving same Strouhal number $St_D = 0.19$ as in our study. The characteristics measured by Taylor et al. (2011) [31] are approximative characteristics as the detection of the vortex core was subjected to the error in the vorticity measurement by PIV. Indeed, they approximated the vortex core by considering that it is delimited by 1% drop on the maximum local vorticity. All the characteristics measured by Taylor et al. (2011) [31] are displayed in table 8. At $Re_c = 4.8 \times 10^5$, for vortex 2 we measure $A/D^2 = 0.72 \pm 0.23$, which is in good agreement with the A/D^2 measured by Taylor et al. (2011) [31].

St_D	A/D^2	$\lvert\Gamma\rvert_{max}/U_0D$
0.19	0.78	1.7

Table 8: Characteristics of the wake vortices measured at X/D=2 and $Re_D = 3.0 \times 10^4$. Geometry with triangular edges of $c/D = 7$, Taylor et al. (2011) [31].

6.4.2. Rotation rate

Figure 23 presents the evolution of the non dimensional rotation rate of modes 1 vortices according to the Reynolds numbers. The rotation rate has been scaled by the vortex shedding frequency f_{vs} measured at each Reynolds. The rotation rate is in between f_{vs} and $5f_{vs}$ and there is a decay of the rotation rate of the vortices (from vortex 1 to vortex 3) in the downstream direction. In the regime out of resonance, the rotation rate of the vortices doesn't vary significantly with the Re_c number. It is obviously imposed by the vortex shedding frequency, and thus by both the upstream velocity U_0 and the Strouhal number St. A sharp decrease of the normalized rotation rate happens at the lock-in with the twisting mode.

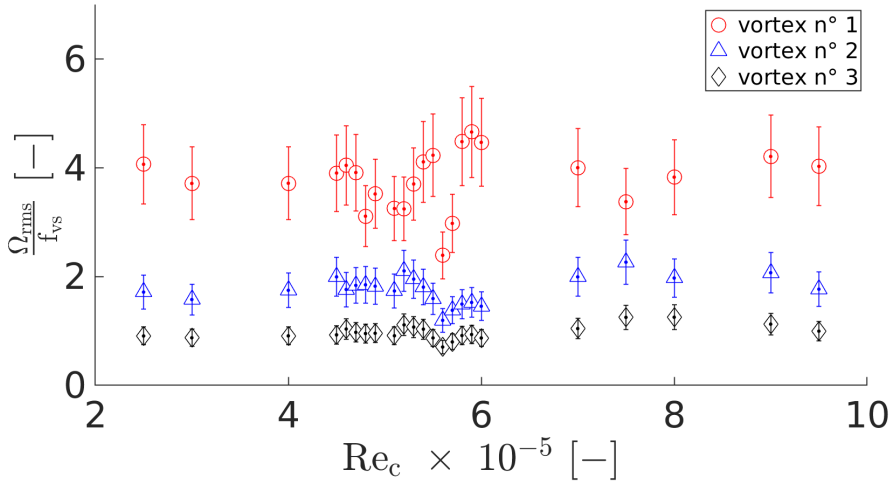

Figure 23: Rotation rate evolution with the Reynolds of the three first vortices downstream the trailing edge (mode 1). The rotation rate is scaled by the vortex shedding frequency. Vortex 1 is the upstream vortex and vortex 3 is the downstream vortex.

6.4.3. Circulation

The vortex circulation downstream of an immersed structure induces an opposite circulation along the structure which results in a lift force. In a potential flow, the lift coefficient C_L is directly linked to the circulation Γ of the vortices in the wake. It yields:

$$\mathrm{C_L} = \frac{2\Gamma}{\mathrm{U_0.c}} \tag{20}$$

For the flat plate at zero incidence, the mean value of $\mathrm{C_L}$ is expected to be zero but the vortex shedding of the Karman wake induces alternative positive and negative $\mathrm{C_L}$ values. Therefore, Γ_{rms} of the Karman vortices scaled by $\frac{\mathrm{U_0 c}}{2}$ gives the magnitude of the rms value of C_L: $\mathrm{C_L^{rms}} = 2\Gamma^{\mathrm{rms}}/\mathrm{U_0 c}$. In figure 24, the normalized values of Γ_{rms} have been plotted with regard to the Reynolds number for the three first vortices of mode 1. It appears that the rms value of the circulation of the vortices seems to converge downstream for vortices 2 and 3, which confirms the relationship between Γ of these two vortices and $\mathrm{C_L}$. This is also in agreement with the decay of the rotation rate and the expansion of the size of the vortices observed downstream of the plate. The lock-in regime can be associated with an abrupt increase of $\mathrm{C_L^{rms}}$ to reach a maximum value at Reynolds ranging between 5.6×10^5 and 5.7×10^5 which corresponds to the maximal structural vibration amplitude. Due to this high lift coefficient value, the structure will endure high level efforts resulting in high amplitude structural deformation in the transverse vertical direction. Vortex 2 and 3 also depict an increase in $\mathrm{C_L^{rms}}$ at the resonance regimes (lock-off resonance of the twisting mode and lock-in with the bending mode). For the Reynolds number range of the study and for the studied geometry of the plate, the $\mathrm{C_L^{rms}}$ of vortices 2 and 3 is of the order of 0.12 in the regimes out of resonance.

Generally speaking, there is a great discrepancy in C_L^{rms} measured in turbulent shedding condition downstream cylinders (Norberg (2001) [30]) and data of C_L^{rms} are not available for flat plates of large aspect ratio in the literature survey. However, we can compare our value of C_L^{rms} to $\frac{|\Gamma|_{max}}{U_0 D}$ measured by Taylor (2011), see table 8. In the work of Taylor, $|\Gamma|_{max}$ is the circulation of each vortex passing at $X/D = 2$, averaged among all the vortices at this position. Our approach is different as Γ_{rms} is the root mean square value in the POD mode 1. The relationship between Γ^{rms} and $|\Gamma|_{max}$ is $\Gamma_{rms} = \frac{|\Gamma|_{max}}{\sqrt{2}}$ when considering that the expansion coefficient $a_1(t)$ varies like a perfect sinusoid with time. For vortex 2 we obtain $\frac{|\Gamma|_{max}}{U_0 D} = 1.4$.

Taylor et al. (2011) [31] have measured a value of $\frac{|\Gamma|_{max}}{U_0 D} = 1.7$ which is same order of magnitude as the value we measure. This means that the circulation of the primary vortices for $X/D > 2$ is imposed by the Strouhal and Reynolds numbers in the non resonance regime.

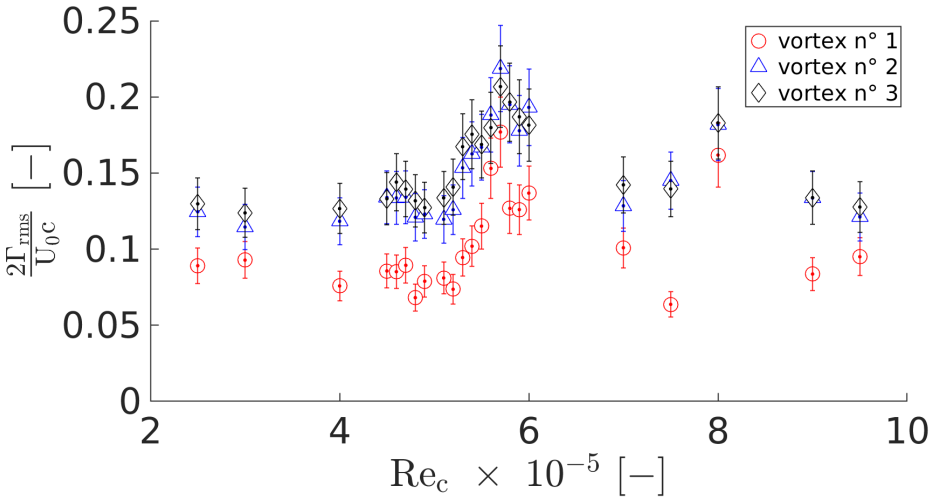

Figure 24: Mode 1 rms circulation evolution with Reynolds of the three first vortices downstream of the trailing edge (mode 1). The circulation is scaled by $\frac{U_0 c}{2}$, which is representative of the lift coefficient. Vortex 1 is the upstream vortex, vortex 3 is the downstream vortex.

The next part of our study will analyse the structure of the different POD modes present in the near wake at the previously defined vibration regimes.

7. Specificity of the POD modes in the near wake for different vibration regimes

This section aims at analysing the main differences in the 9 different POD modes observed in the near wake of the plate for the three points of interest (A), (B), (C) summarized in table 7 and characteristic of the three vibration regimes: out of resonance, lock-off resonance and lock-in. For the purpose of the analysis, the first part of this section is dedicated to physical background of reattached flows.

7.1. features of the TKE distribution according to $\mathrm{Re_c}$ *number*

Figure 25 displays the number of modes $N_{90\%}$ necessary to reach 90 % of total TKE. In general, without fluid-structure interactions, $N_{90\%}$ increases with the Reynolds number. Indeed, higher level of turbulence implies a broader distribution of the energy among the modes because of the contribution of various length scales proper to turbulent flows, Miyanawala et al. (2019) [39]. This trend is obviously observed for Reynolds numbers out of resonance. In the present study, due to fluid-structure interaction, the lowest value of $N_{90\%}$ is attained for Reynolds ranging between 5.7×10^5 and 6.0×10^5 which corresponds to the lock in regime with the twisting mode. A local minimum is also observed at $Re_c = 8 \times 10^5$ corresponding to the lock-in with the second bending mode.

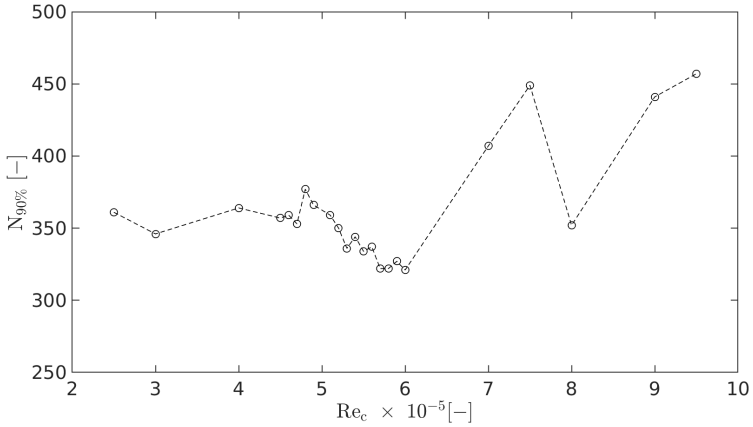

Figure 25: Number of modes to reach 90% of the total energy according to Reynolds number.

Figure 26 presents the energy of the nine first modes as a percentage of the total energy for the three studied vibration regimes. These nine first modes account at least for 47% of the total energy. For this reason, in the following, we will limit the analysis to the nine first modes. It appears that the highest energy percentages are associated with modes 1 and 2 as these modes cumulate on there own more than 35 percent of the total energy. During the lock-in regime ($Re_c = 5.7 \times 10^5$), the cumulated energy percentage of modes 1 and 2 reaches 44 percent of the total energy. Coupling with the high amplitude structural vibration, specific to this regime, is responsible of a strengthening of the first two modes. The cumulated energy of modes 3 to 9 decreases at resonance and particularly at the lock-in, demonstrating the fact that there is a redistribution of the energy from the high order modes to the low order modes at lock-in. See table 9 for a synthesis of the cumulated energy.

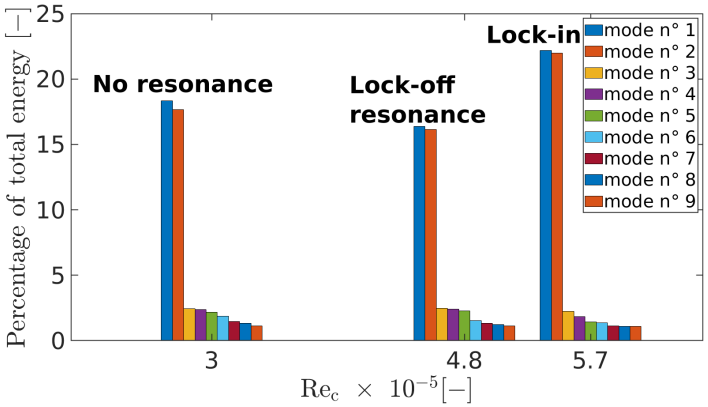

Figure 26: Respective percentage of the total energy of the 9 first POD modes for each studied vibration regime.

Vibration regime	**(A)**	**(B)**	**(C)**
$\mathrm{Re_c}$	3.0×10^5	4.8×10^5	5.7×10^5
Number of modes to reach 90% of total energy	346	377	322
Cumulated energy modes 1 to 2	36.0%	36%	44.1%
Cumulated energy modes 3 to 9	12.8%	11.6%	10.2%
Cumulated energy modes 1 to 9	48.8%	47.6%	54.3%

Table 9: Synthesis of cumulated mode energy distribution of the 9 first POD modes for each studied vibration regime.

7.2. Physical background of reattached turbulent flows

Associating physical phenomena to POD spatial modes at high Reynolds can be challenging as the large-scale coherent structures are impacted by the smaller scale wake features proper to fully turbulent flows. This results in a bombardment of the wake patterns by turbulence inducing some spatial distortion of the modes. For a blunt plate with square leading edge of chord to thickness ratio $6 \leq c/D \leq 36$ and for thickness based Reynolds numbers Re_Din the range $[1.5 \times 10^4 - 7.5 \times 10^4]$, a laminar separation bubble (LSB) has been systematically observed with a length $L_R/D = 4.2 - 5$, Taylor et al. (2011) [31], Taylor et al. (2014) [10], Zhang et al. (2017) [40], Hu et al. (2018) [41], Cherry et al. (1984) [42]. For $c/D \geq 6$, which is the case of our study, the size of the LSB is not dependent on c/D as it is systematically reattached at the same position which rather depends on the Reynolds number. The thickness of the turbulent boundary layer at the separation from the trailing edge depends on both the Reynolds number and c/D. For the Re_D number range of our study, we can consider that $L_R/D \approx 4.5$ is a good approximation. Different periodic mechanisms taking place in the boundary layer can influence the near wake (Cherry et al. [42]):

- Low frequency flapping of the leading edge separation with a characteristic Strouhal number. $St_D^f = f_f D/U_0 \approx 0.02 - 0.03$ where f_f is the characteristic frequency of the flapping.
- LSB vortex shedding of characteristic Strouhal numbers $St_R = f_R L_R/U_0 \approx 0.6 - 0.7$ and $St_{RD} = f_R D/U_0 \approx 0.12 - 0.14$, where f_r is the LSB vortex shedding frequency. This can induce a phenomenon referred as impinging leading edge vortices (ILEV).

For important c/D ratios, the ILEV is expected to be strongly reduced, Zhang et al. (2017) [40], because of the important diffusion of the leading edge vortices. However, the chord to thickness ratio $c/D = 16$, which corresponds to the geometry of the study, is at the transition of two mechanisms: either the impinging leading edge vortices or the trailing edge vortex shedding could be the major mechanism of influence for the vortex shedding and induced vibrations, Kaneko et al. (2008) [43]. If the main mechanism is the trailing edge vortex shedding, then the Strouhal number is in agreement with the Strouhal number of bluff bodies $St_D \approx 0.2$. The trailing edge induced instability (TEI) in the near wake of bluff bodies has been studied recently by Sevilla et al. (2004) [44] based on linear stability theory. Interestingly, the thickness based Strouhal number St_D value evolves with the streamwise distance from the trailing edge from 0.1 to 0.23. Maximum instability is found in the recirculating region of the near wake for $0.3 \leq X/D \leq 1$, which gives rise to St_D in the range $[0.09 - 0.15]$.

As a summary, we can consider that the Strouhal number of ILEV shedding and the one associated to trailing edge instability (TEI) are same order of magnitude $St_D \approx 0.1 - 0.2$. The Strouhal number of the flapping of the shear layer separation is one order of magnitude lower $St_D \approx 0.02$.

7.3. Identification of the physical modes

In order to facilitate the identification of physical modes, we propose to base our analysis of the first 9 modes on both:

- The symmetry or anti-symmetry of the vorticity distribution of the modes in the (x,y) plane according to the wake centreline.
- The time evolution and the dominant frequencies exhibited by the frequency spectrum of their expansion coefficients $a_k(t)$.

These criteria have been applied to the 9 first modes at each vibration regime. The physical mode identification method based on symmetry is inspired from the work proposed by Miyanawala et al. (2019) [39] for the study of a square cylinder at low to moderate Reynolds number. We can consider that antisymmetry of the vorticity distribution is characteristic of shear layer modes (SL) and near wake bubble (WB) mode i.e recirculation region of the wake. Symmetry distribution is characteristic of the Karman vortex shedding (KVS). The analysis of the dominant frequencies of the different modes will help in identifying the contribution of possible flapping, ILEV or TEI.

7.3.1. Non resonance regime

The non resonance regime studied at $Re_c = 3.0 \times 10^5$ is associated with low magnitude vibrations. As a consequence there should be weak influence of the vibrations on the wake. This case is used as a reference for comparison with resonant regimes. Figure 28 presents the vorticity cartography of the 9 first modes. As discussed in section 6, modes 1 and 2 are symmetric modes of highest vorticity which are characteristic of the Karman vortices. Also, by regarding the frequency spectrum of the POD coefficients on figure 27, it appears that modes 1, 2 and 9 have a similar well established dominant frequency equal to the Karman vortex shedding frequency of 93 Hz. The spatial distributions associated to modes 3 to 9 do not highlight a well defined structure, so the identification is not simple. Mode 8 exhibit a broadband spectrum of maximum TKE around the expected flapping frequency, which is in the range [10-15] Hz (for $St_D^f = 0.02 - 0.03$). In mode 8, the highest vorticity region is located in the wake bubble and mode 8 is thus characteristic of the flapping of the wake bubble, as a consequence of the flapping of the separated shear layer. Mode 8 is thus identified as a wake bubble mode (WB mode). The vortex shedding from the LSB is expected to be in the range 60-80 Hz. No peaks in the spectra of the expansion coefficient are clearly evidenced for this frequency range. However, very large band spectra are observed for modes 3, 4, 5 in the frequency range [50-100] Hz. This frequency range is characteristic of the trailing edge instability (i.e $St_D = 0.1 - 0.2$). No clear structure is evidenced on the vorticity maps of these modes. Modes 3, 4 and 5 are identified as TEI modes. Other modes results from the combination of WB and TEI modes, KVS modes and their harmonics. They are preferentially identified as TEI modes. Note that the time evolution of the expansion coefficients of the KVS modes $a_1(t)$ and $a_2(t)$ shows a modulation of the Karman vortices at a small frequency, which is same order of magnitude as the flapping frequency.

For highly turbulent flows, as evidenced by Miyanawala et al. (2019), the identification method fails. As expected, for this regime out of resonance, the identification of physical POD modes is very difficult.

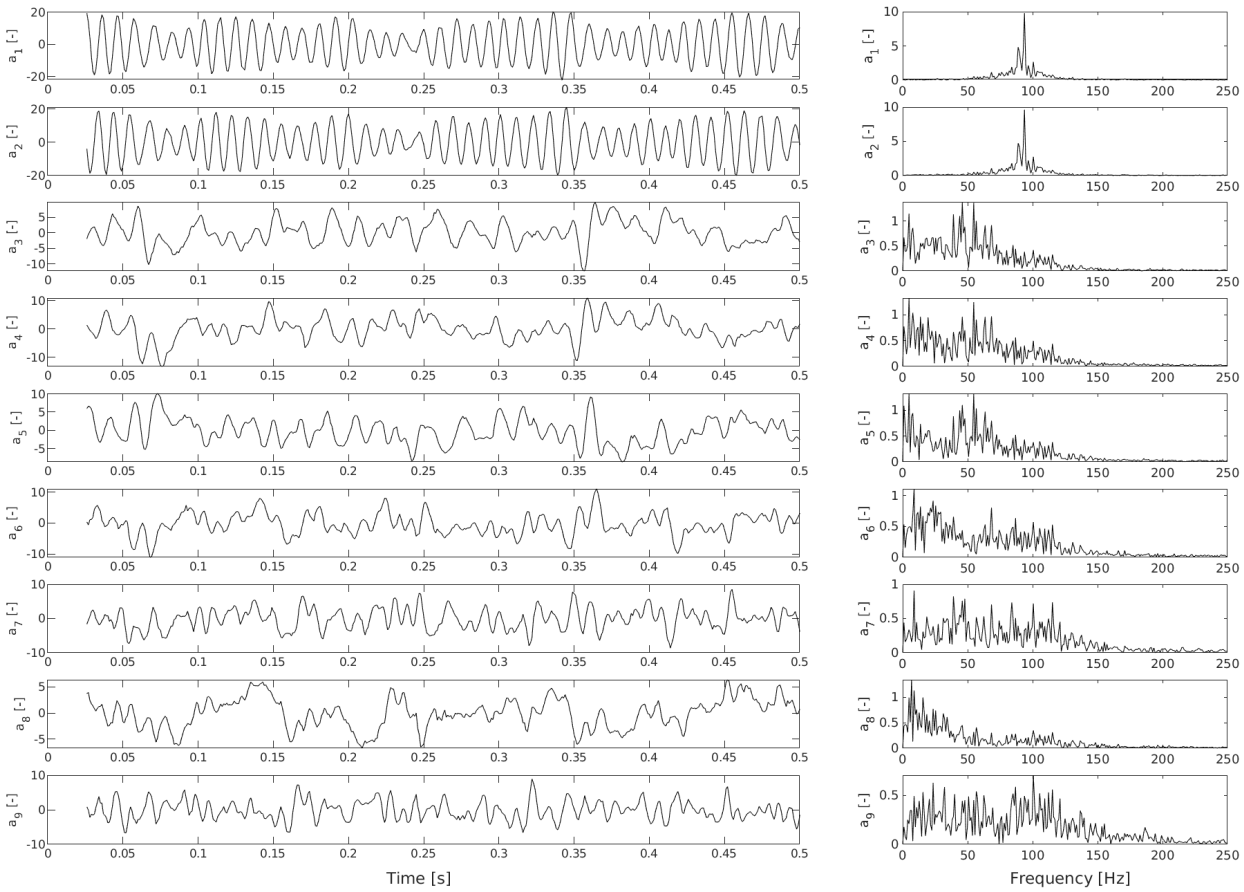

Figure 27: Temporal coefficients and associated frequency spectrum of POD modes 1 to 9 at $U_0 = 3.0\ m.s^{-1}$.

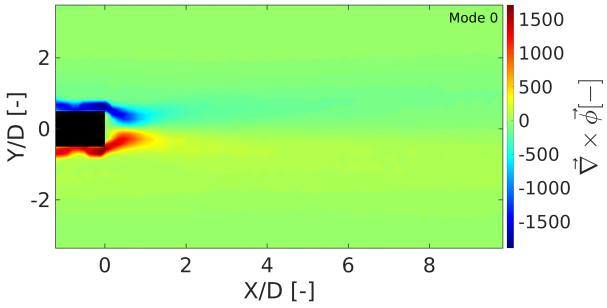

(a) Mean vorticity field

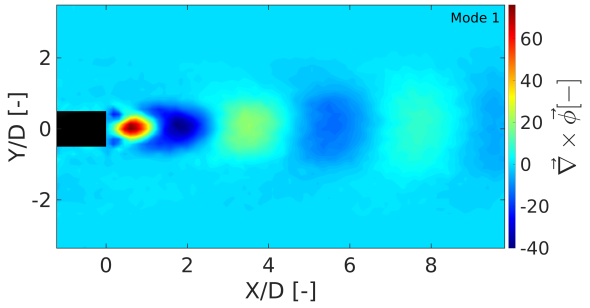

(b) Mode 1 (18.35 %): KVS

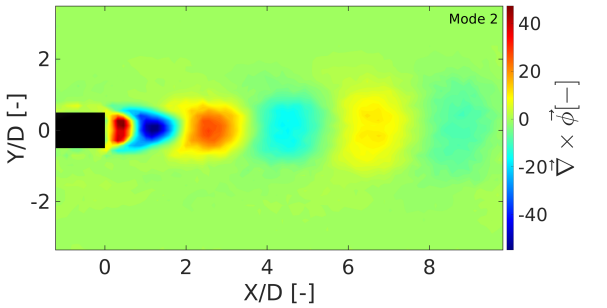

(c) Mode 2 (17.65 %): KVS

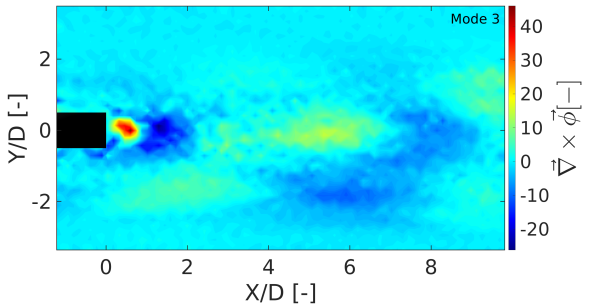

(d) Mode 3 (2.43 %): TEI

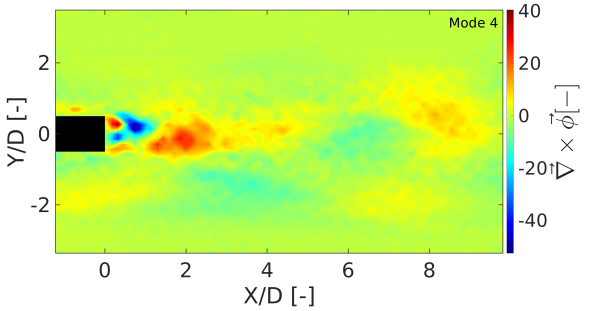

(e) Mode 4 (2.39 %): TEI

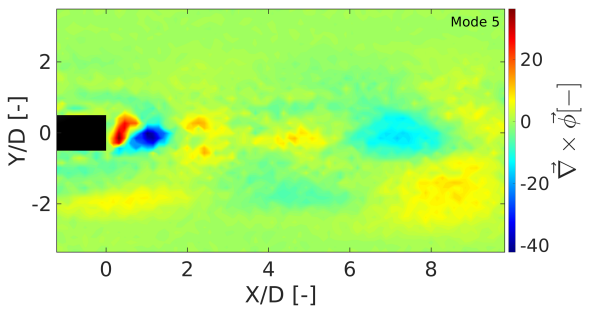

(f) Mode 5 (2.19 %): TEI

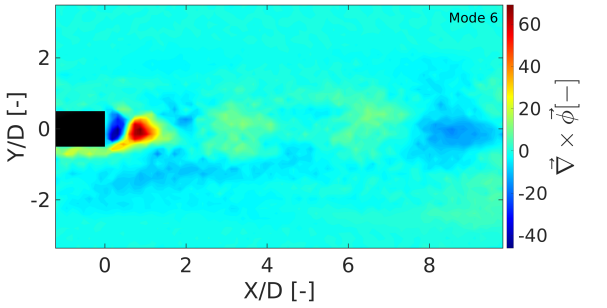

(g) Mode 6 (1.88 %): TEI

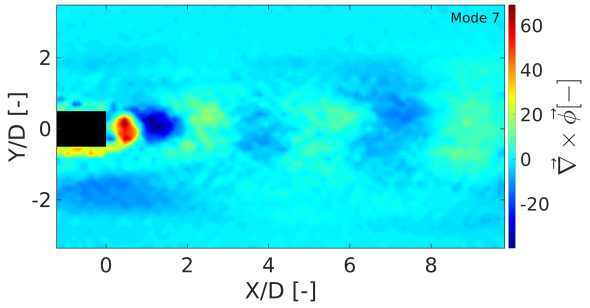

(h) Mode 7 (1.46 %): TEI

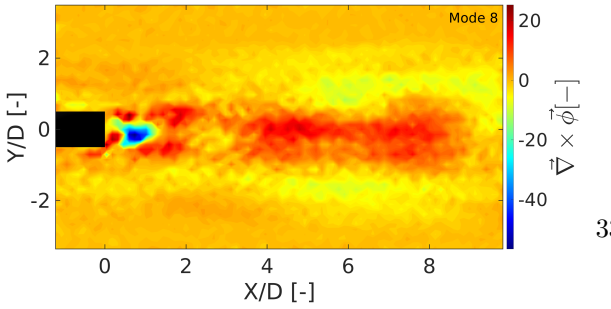

(i) Mode 8 (1.34 %): WB

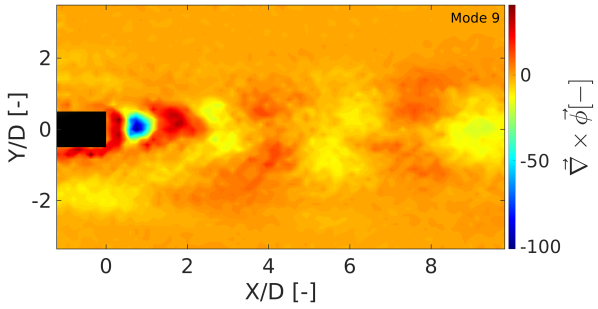

(j) Mode 9 (1.14 %): TEI

Figure 28: (x,y) cartography of vorticity. Mean vorticity field and spatial POD modes from 1 to 9 at $U_0 = 3.0\ m.s^{-1}$.

7.3.2. Lock-off resonance regime

The lock-off resonance regime studied at $Re_c = 4.8 \times 10^5$ is characterized by a local maximum amplitude of vibrations at a frequency equal to the natural frequency of the twisting mode f_2 but with an excitation frequency f_{vs} that is still different from f_2. As demonstrated by figure 30, modes 1 and 2 are still the most energetic ones and are still representative of the Karman vortex shedding at $f_{vs} = 160\ Hz$ for this Re_c. The spatial distribution of modes 3 and 5 is symmetric and is very similar to the one of modes 1 and 2 but it exhibits one more vortex than modes 1 and 2 in the stream wise direction. This is coherent with the fact that the dominant frequency of modes 3 and 5 is higher than the one of modes 1 and 2, it is equal to the twisting mode natural frequency $f_2 = 182\ Hz$. Modes 3 and 5 are then identified as a second Karman mode: they represent Karman vortices locked at f_2.

This observation is proper to the lock-off resonance and it demonstrates the fact that two dominant frequencies coexist in the Karman wake: f_{vs} and f_2. When looking at the time evolution of $a_1(t)$, $a_2(t)$, $a_3(t)$ and $a_5(t)$ it seems that modes 3 and 5 alternate with modes 1 and 2 leading to intermittency of the Karman wake vortex shedding at f_{vs} and f_2. In addition, the phase diagram of $(a_1 - a_2)$ (figure 21 b) for this regime shows that modes 1 and 2 are much less phase corelated than for the other regimes. The difference $f_2 - f_{vs} = 22\ Hz$ is in agreement with the expected value of the flapping frequency of the separated layer (Strouhal number of $St_D^f = 0.027$). We can infer that the flapping which modulates the Karman vortex shedding is responsible for the emergence of this alternative Karman vortex shedding mode, locked at f_2.

An other important feature is the emergence in mode 4 of an antisymmetric structure which is identified as the wake bubble. This observation is of great interest as it seems to be the particularity of a resonance regime. Mode 4 is characterized by a low frequency broadband spectrum of maximum TKE at the flapping frequency $f_f = 22\ Hz$. This is consistent with the flapping of the wake bubble. Mode 6 is the harmonic of the flapping wake bubble. Thus modes 4 and 6 are identified as WB modes. Modes 7, 8 and 9 are identified as modes of interaction between the trailing edge instability of frequency within $[80 - 160]\ Hz$ and the bubble wake flapping and thus identified as TEI modes.

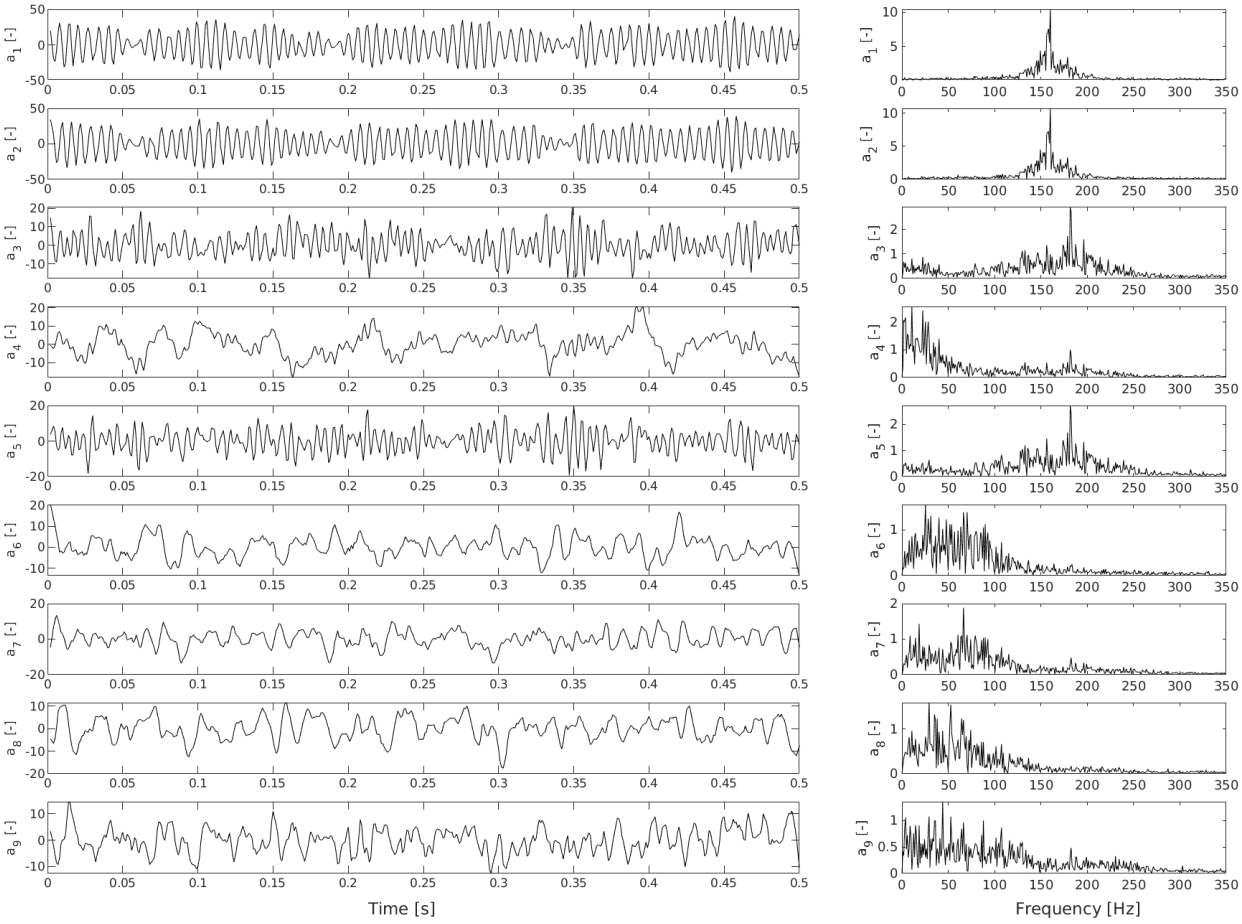

Figure 29: Temporal coefficients and associated frequency spectrum of POD modes 1 to 9 at $U_0 = 4.8\ m.s^{-1}$.

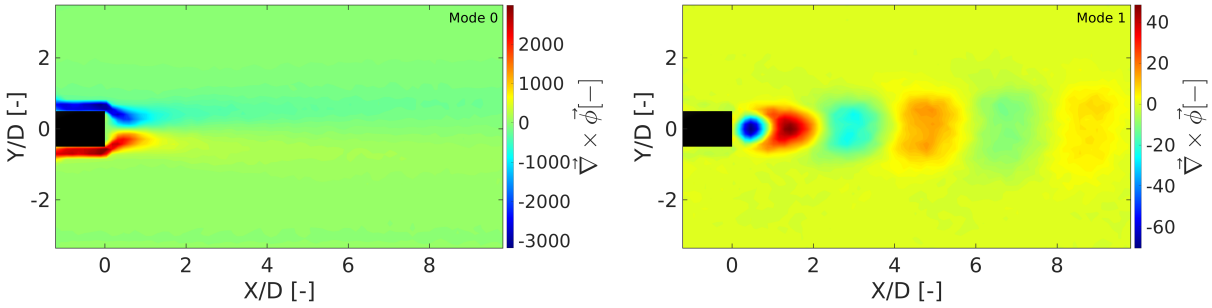

(a) Mean vorticity field

(b) Mode 1 (16.38 %): KVS1

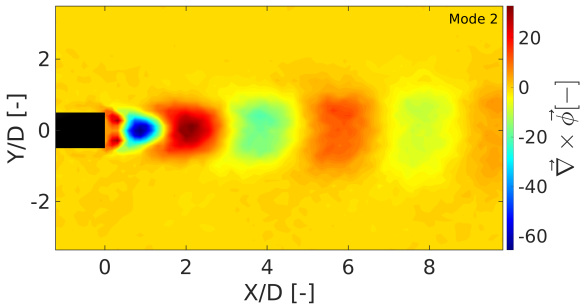

(c) Mode 2 (16.15 %): KVS1

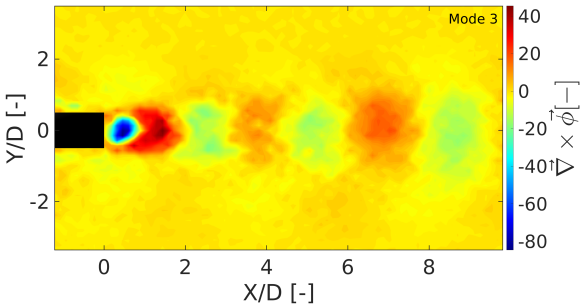

(d) Mode 3 (2.49 %): KVS2

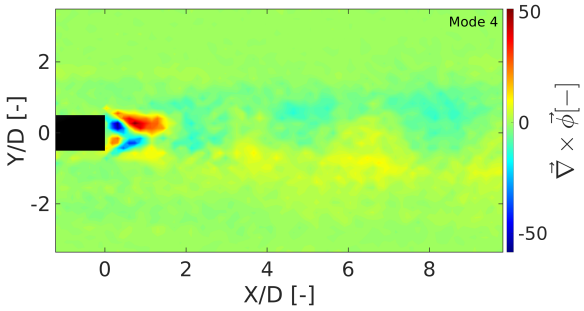

(e) Mode 4 (2.43 %): WB

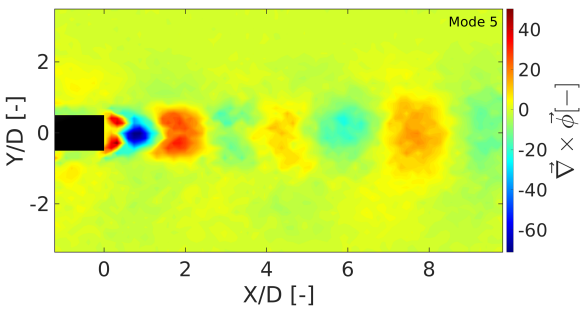

(f) Mode 5 (2.26%): KVS2

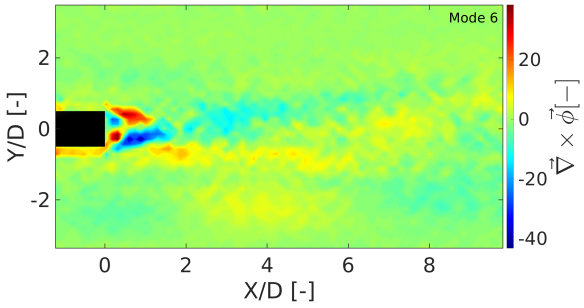

(g) Mode 6 (1.54 %): WB

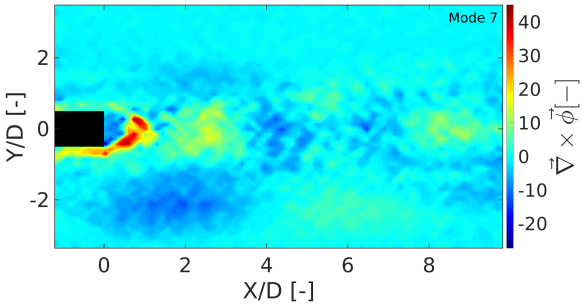

(h) Mode 7 (1.34 %): TEI

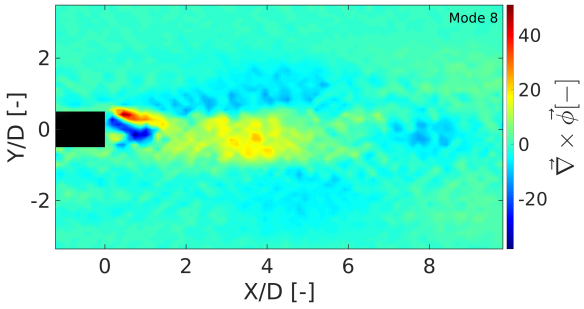

(i) Mode 8 (1.23 %): TEI

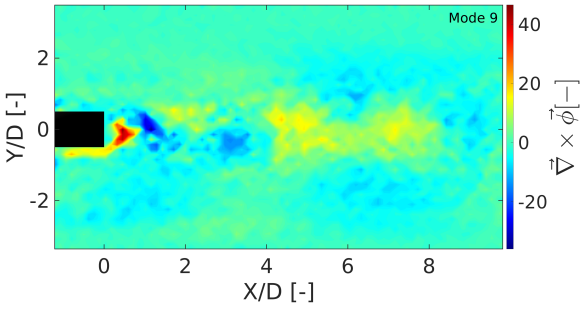

(j) Mode 9 (1.11 %): TEI

Figure 30: (x,y) cartography of vorticity. Mean vorticity field and spatial POD modes from 1 to 9 at $U_0 = 4.8\ m.s^{-1}$.

7.3.3. Lock-in regime

The lock-in regime occurring at $Re_c = 5.7 \times 10^5$ is characterized by the highest amplitude vibrations at a frequency equal to the Karman vortex shedding frequency. Major fluid structure interaction is expected to occur at this regime due to an important energy transfer from the wake to the structure. As presented by figure 32 modes 1 and 2 are still representative of symmetric Karman vortex shedding. The time evolution of their expansion coefficient shows a periodic behaviour with the highest phase correlation between a_1 and a_2 (figure 21 c) by comparison to the other vibration regimes. In comparison with the previous regimes an enlargement of the wake in the Y direction is visible. This also happens for mode 3 which still represents the shear layer. A particular feature of this regime is the appearance of a very well defined coherent and antisymmetric structure visible on modes 8 and 9. These modes evidence propagative coherent structures developing at the corner of the trailing edge. These modes will be identified as shear layer vortex shedding modes (SLVS).The spectrums of the pod coefficients of these modes are narrow banded similarly to the ones of modes 1 and 2 and have a dominant frequency equal to twice the vortex shedding frequency of Karman modes ($f_{7,8,9} = 2 \times f_{vs} = 2 \times f_2$). This feature, in combination with the presence of a shear layer and with the wake enlargement seems to be the key specificity of the lock in regime. These modes are identified as shear layer vortices at the harmonic of the Karman frequency which is expected to modulate the drag force.

At $Re_c = 5.7 \times 10^5$, a Strouhal number $St_D^f = 0.025 - 0.027$ gives a characteristic value of the flapping frequency in the range 24-26 Hz. This is same order of magnitude as the dominant frequency of mode 3 which is the low frequency mode. The vorticity map of mode 3 exhibits the structure of the wake bubble near the trailing edge as well as residual vorticity downstream of the boundary of the wake. Mode 3 results from the flapping of the separated shear layer and is preferentially identified as wake bubble WB mode. This kind of mode has been enlarged in the Y direction for this vibration regime. No clear peak at the ILEVS frequency of $f_R \approx 114 - 142\ Hz$ (for $St_{DR} \approx 0.12 - 0.14$) is evidenced on the different modes.

Other modes 4, 5, 6 are combinations between the Karman vortices modes, the wake bubble, flapping modes and its harmonics and the TEI which is expected in the frequency range [95-190] Hz. Mode 4 is identified as preferential WB mode as much of its TKE is contained in the harmonics of the flapping. Modes 5 and 6 are identified as preferential TEI modes.

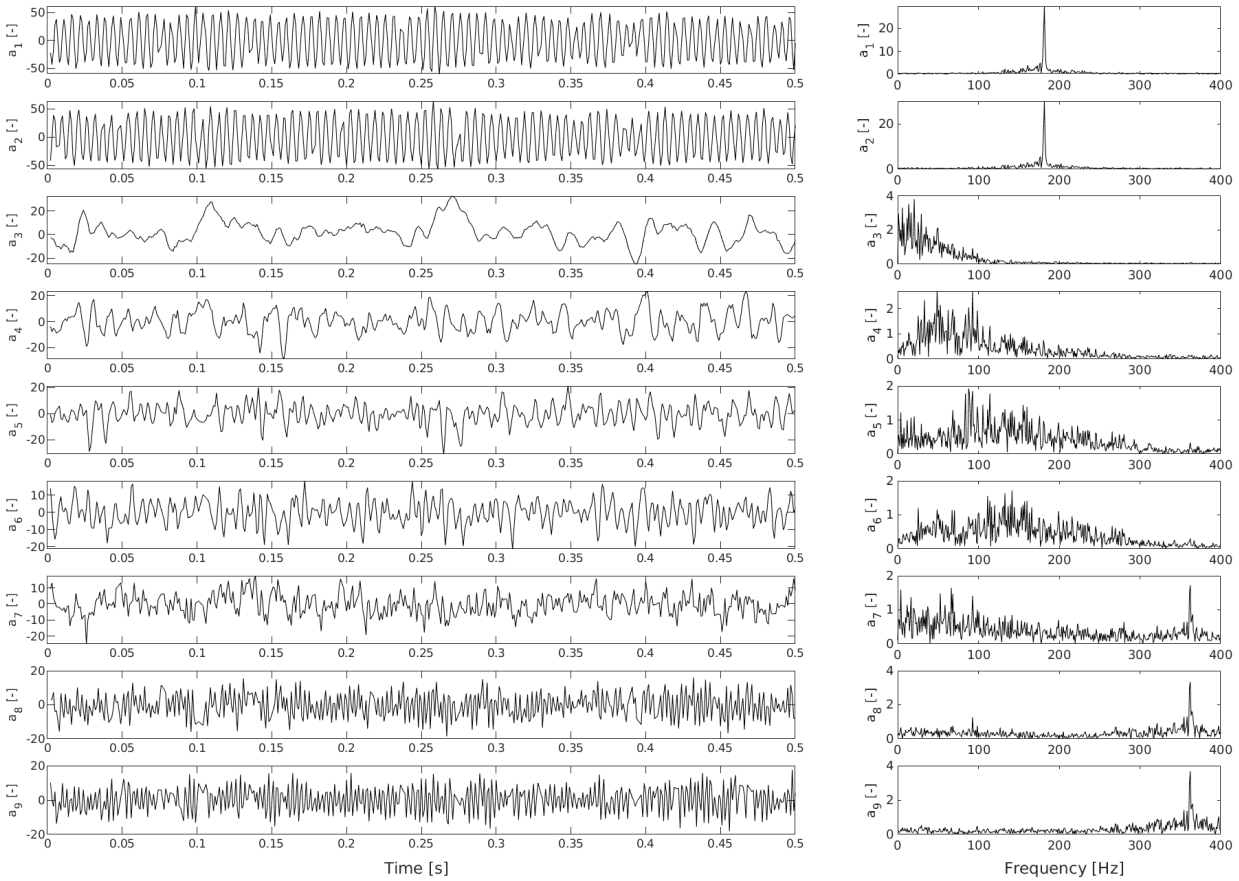

Figure 31: Temporal coefficients and associated frequency spectrum of POD modes 1 to 9 at $Re_c = 5.7 \times 10^5$.

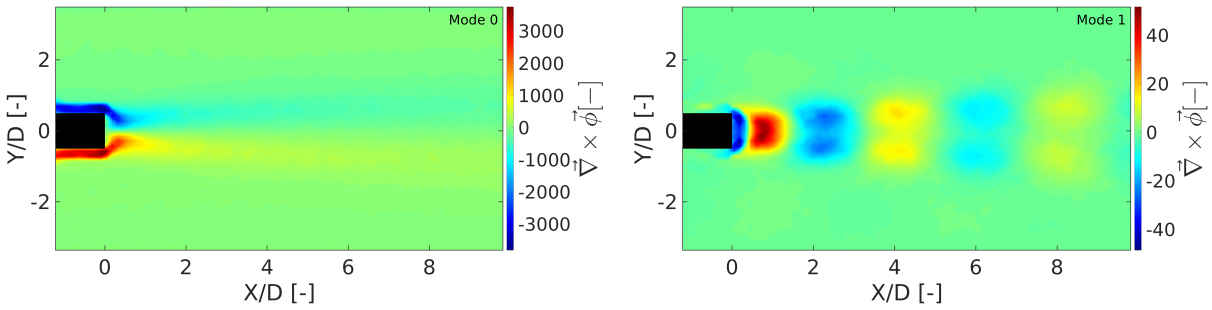

(a) Mean vorticity field

(b) Mode 1 (22.18 %): KVS1

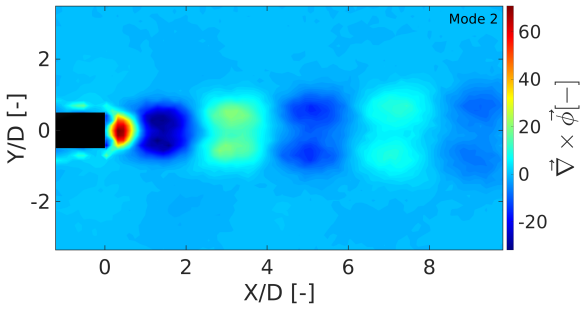

(c) Mode 2 (21.98 %): KVS1

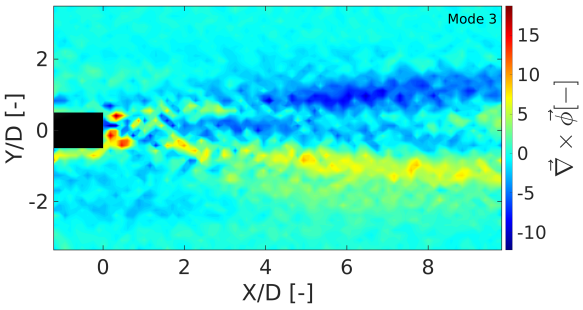

(d) Mode 3 (2.25 %): WB

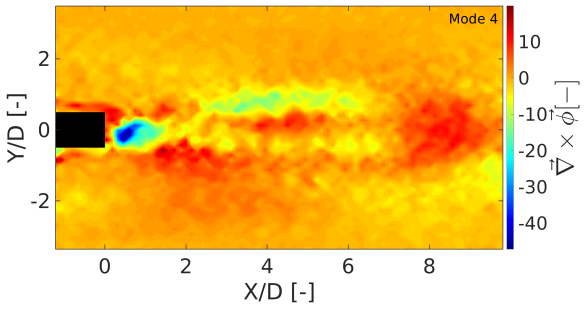

(e) Mode 4 (1.85 %): WB

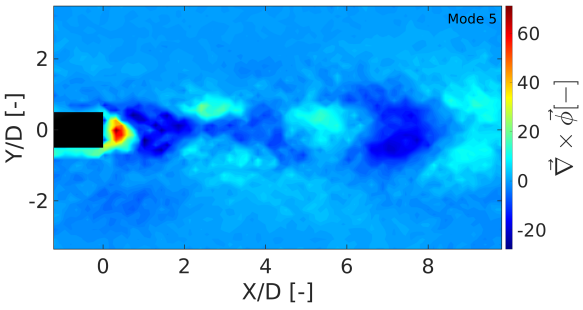

(f) Mode 5 (1.42 %): TEI

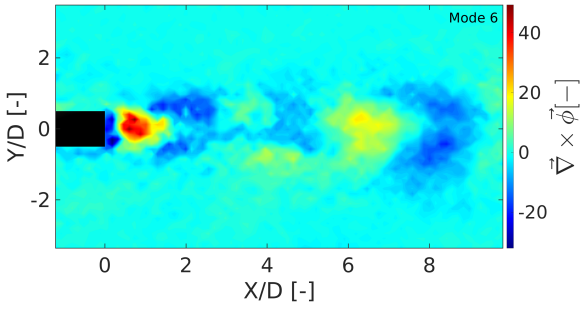

(g) Mode 6 (1.35 %): TEI

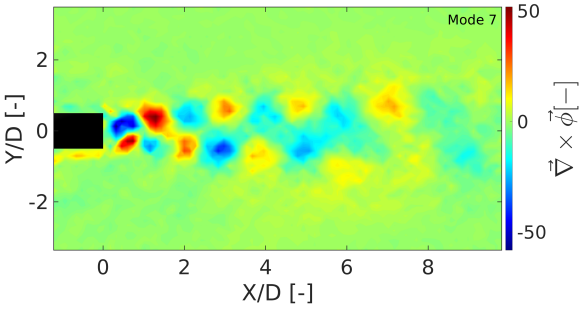

(h) Mode 7 (1.13 %): SLVS

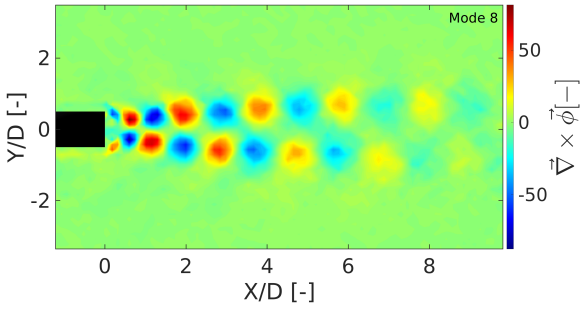

(i) Mode 8 (1.09 %): SLVS

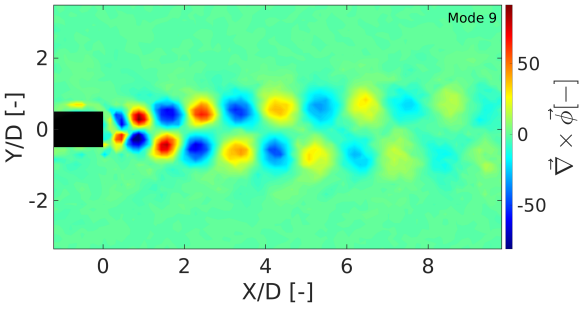

(j) Mode 9 (1.09 %): SLVS

Figure 32: (x,y) cartography of vorticity. Mean vorticity field and spatial POD modes from 1 to 9 at $Re_c = 5.7 \times 10^5$.

7.3.4. 2S and 2P vortex shedding

Figure 33 (a) presents a snapshot of the vorticity in the plane (x,y) at the non-resonance regime. The combination of all 9 first modes shows a typical structure which is called 2S shedding. This type of shedding is characteristic of out of resonance regimes or resonance regimes at small vibration amplitudes. It consists of one pair of counter rotating vortices shed by cycle of vibration. Similarly, figure 33 (b) displays a snapshot of the vorticity in the plane (x,y) at lock-in. The combination of all 9 first modes depicts the existence of a $2P_0$ structure for $X/D > 4$. This typical structure is composed of two pairs of counter rotating vortices shed by cycle of vibration. This is the same kind of structure as what is called 2P structure but the difference is that the secondary vortex in each pair is weaker than the primary vortex. 2P and $2P_0$ structures are characteristic of vortex shedding in the near wake of bluff bodies of high vibration amplitude. As explained by Morse et al. (2009) [45], $2P_0$ is some kind of transition between 2S and 2P mode. To our knowledge, this kind of near-wake structure has never been evidenced and analysed in case of a blunt plate.

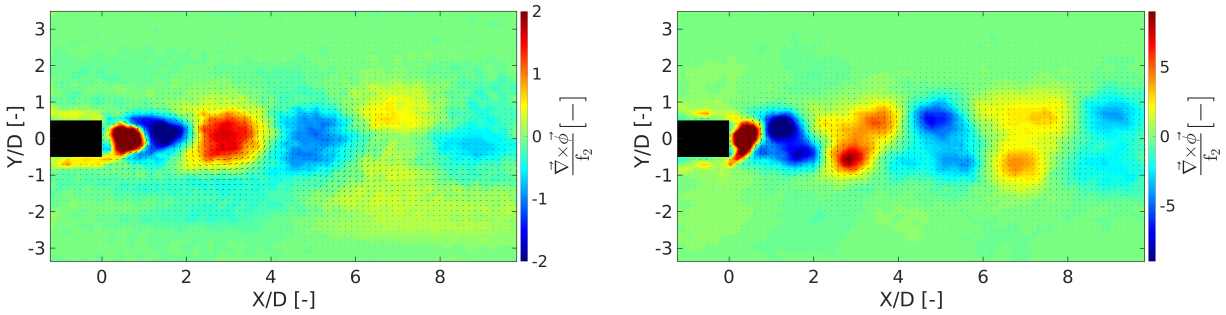

(a) No resonance: 2S vortex shedding

(b) Lock-in: $2P_0$ vortex shedding

Figure 33: Snapshot of the (x,y) cartography of the reconstructed vorticity, including modes 1 to 9 at (a) the non resonance regime ($Re_c = 3.0 \times 10^5$) and (b) the lock-in regime ($Re_c = 5.7 \times 10^5$).

8. Discussion on the fluid structure interaction mechanism at resonance

The fluid structure interaction mechanism at resonance is highly influenced by the Karman vortices and the shear layer. Shear layers, are known to be unstable and dependent of small perturbations which results in a reciprocating widening of the shear layer, Miyanawala et al. (2019) [39]. Accordingly, the shear layer is highly dependent to the structural vibrations because these acts as a perturbation source. In order to appreciate the energy transfer between the various types of modes at the different vibration regimes of the structure, figure 34 summarizes the contributions to the total TKE of the different physical identified modes (Karman vortex shedding KVS, shear layer vortex shedding SLVS, wake bubble BW and trailing edge instability TEI). KVS1 is the Karman vortex shedding at f_{vs} (given by $St_D = 0.195$) while KVS2 is the second karman vortex shedding mode at $f_2 \neq f_{vs}$. Modes containing 0% TKE are not plotted in this figure as it is a logarithmic plot.

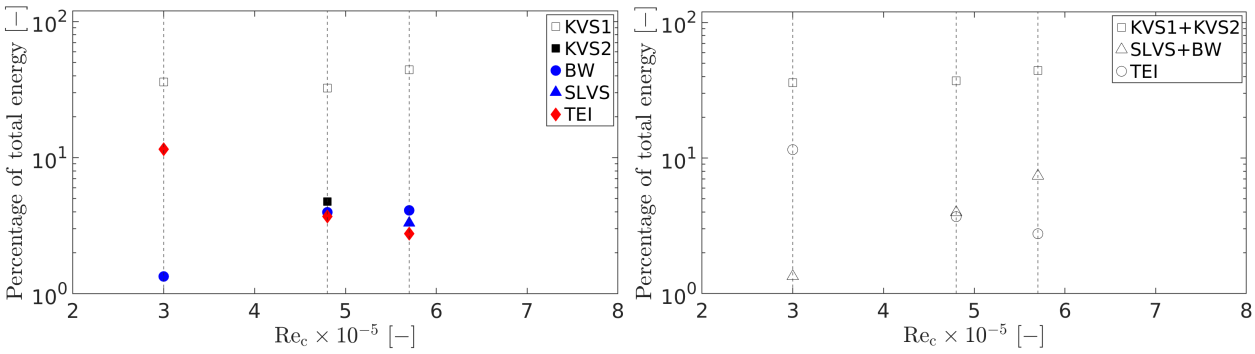

(a) Physical modes

(b) Force modes

Figure 34: TKE contributions of the different physical identified modes and force modes with respect to the vibration regime. Modes containing 0% TKE are not plotted in this figure as it is a logarithmic plot.

The vortex shedding energy (KVS1) reaches a maximum at the lock-in resonant regime. The resonant regimes (lock-off resonance and lock-in) are characterized by a decrease in the trailing edge instability (TEI) contribution, which is the energy of the non-clearly structured wake, in favour of the energy contained in the flapping of the bubble wake (BW). The BW energy is multiplied by a factor 2 and a factor 3 respectively for the lock-off resonance and lock-in resonance regimes respectively. Flapping of the BW is enhanced by the twisting motion of the plate at resonance which better correlates in phase both motions of leading and trailing edges. The occurrence of resonance at the lock-off resonance comes from the lock-in of the plate of the flapping induced modified Karman vortex shedding (KVS2 mode) with the twisting mode .

The strong vibration generated at the lock-in regime is responsible for the contribution in the 9 first modes of the shear layer vortex shedding mode (SLVS). This mode is responsible of the modulation of the drag force at $2f_{vs}$. Note that this mode exists but contributes at much lower energy levels for the other vibration regimes. At lock-in, the energy contained in this mode contributes to the widening of the shear layer.

The Karman vortex shedding modes, contribute to unsteady behaviour of the lift force, while the wake bubble mode, as well as the shear layer vortices modes, contribute to the unsteady behaviour of the global drag force applied to the plate. The energy levels of these respective contributions (unsteady lift and unsteady drag modes) are plotted in figure 34 b. By comparison to the non-resonant regime at $Re_c = 3 \times 10^5$, we observe an increase of 12% (respectively 22%) of the total energy of the unsteady lift mode which gives rise to an increase of C_L^{rms} of 20% (respectively 80%) for lock-out (respectively lock-in) resonance regimes. C_L^{rms} is deduced from figure 34 b. The contribution of the unsteady drag modes has been increased by 140% at the lock-off resonance and by 450% at the lock-in resonance regime.

For the lock-in regime, this strong augmentation of the unsteady drag is in agreement with the enhancement of the time averaged drag force as expected from:

- The vertical widening of the wake and shear layer.
- The attenuation of the eddy length.
- The increase in the recirculation of the time averaged wake bubble.

Interestingly, at lock-in with the twisting mode of the plate, the transfer between the different modes can be summarized as in Miyanawala et al. (2019). The lock-in phenomenon induces the wake and shear layer widening, which gives rise to a strengthening of the near wake bubble and the Karman vortices through a vorticity transfer. The synchronized vortex shedding with the resonant mode of the structure brings about lock-in. This scenario was evidenced by Miyanawala et al. (2019) for a square cylinder at moderate Reynolds number. For this configuration, the separated shear layer at the leading edge is strongly linked to the wake flow, which simplifies the problem of fluid-structure interactions.

In the case of the blunt plate, with large chord to a thckness ratio, at much higher Reynolds number, the mechanism of fluid-structure interaction is quite similar with the square cylinder because lock-in reduces the disorganization of the near wake. This implies a transfer of energy from the TEI mode to the BW mode at the lock-in. We infer that the mechanism at lock-in which enables this energy transfer is the flapping of the separated shear layer which is enhanced by the high level of strucutre vibration. The enhanced instability of the wake bubble is responsible for the enhanced vorticity of the Karman vortices shed downstream. For the blunt plate at large chord to thickness ratio, we can summarize the mechanism of energy modes transfer in the following figure.

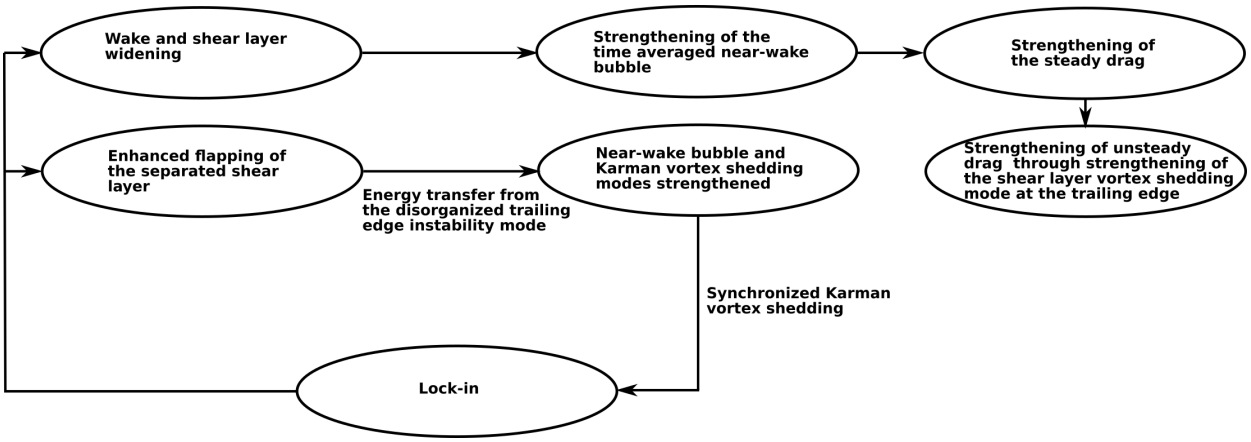

Figure 35: Conceptual sketch of energy transfer at lock-in with the twisting mode of a blunt plate with chord to thickness ratio $c/D = 16$.

9. Conclusion

Acknowledgements

The authors gratefully acknowledge the financial support of...

Appendix A. Vortex detection algorithm

Appendix A.1. Vortex center identification Γ_1

The vortex center identification algorithm has first been introduced by Michard et al. in 1997 [46]. Consider a fixed point P surrounded by a two dimensional surface S in the measurement domain and M, an other point located in S. The dimensionless scalar function Γ_1 at P is expressed as:

$$\Gamma_1(\mathrm{P}) \;=\; \frac{1}{\mathrm{S}} \int_{\mathrm{M}\in\mathrm{S}} \frac{(\mathbf{PM} \wedge \mathbf{U_M}) \cdot \mathbf{z}}{\|\mathbf{PM}\| \cdot \|\mathbf{U_M}\|} \mathrm{dS} \;=\; \frac{1}{\mathrm{S}} \int_{\mathrm{S}} \sin(\theta_{\mathrm{M}}) \mathrm{dS} \tag{A.1}$$

Where $\mathbf{z}$ is the unit vector normal to the measurement plane and θ_{M} represents the angle between the velocity vector $\mathbf{U_M}$ and the radius vector $\mathbf{PM}$. When the velocity field is sampled at discrete spatial locations as presented by figure A.36, S is a rectangular domain of fixed size and geometry centred on P. Accordingly, an approximation of the Γ_1 function is expressed by:

$$\Gamma_1(P) \;=\; \frac{1}{N_p} \sum_{S} \frac{(\mathbf{PM} \wedge \mathbf{U_M}) \cdot \mathbf{z}}{\|\mathbf{PM}\| \cdot \|\mathbf{U_M}\|} \;=\; \frac{1}{N_p} \sum_{S} sin(\theta_M) \tag{A.2}$$

with N_p the number of points M inside S. Graftiaux et al. (2001)[20] have shown that $\|\Gamma_1\|$ is a dimensionless scalar bounded by 1 and that the value of $\mathrm{N_p}$ weakly affects the maximum location of Γ_1

even if it acts as a spatial filter. With this method, local maxima of $mathrm\Gamma_1$ can be identified as vortices centres.

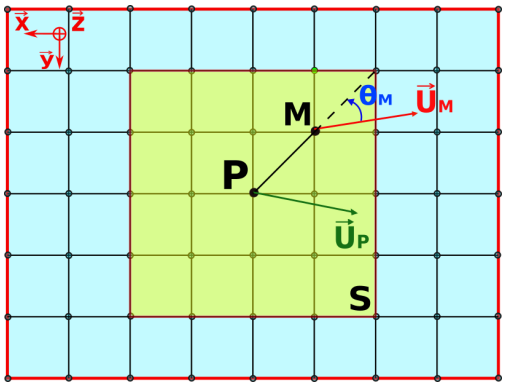

Figure A.36: Schematic view of vortex core identification model on a discretized space.

Appendix A.2. Vortex core identification Γ_2

This methods aims to detect the boundaries of the solid core of the vortices. It is similar to the vortex centre identification method but takes into account a local convection velocity $\mathbf{U_P}$ at P:

$$\tilde{U}_P = \frac{1}{S}\int_S U\, dS$$

Accordingly, the dimensionless scalar function Γ_2 at P is expressed as:

$$\Gamma_2(P) = \frac{1}{S}\int_{M\in S} \frac{[\mathbf{PM}\wedge(\mathbf{U_M}-\mathbf{U_P})]\cdot\mathbf{z}}{\|\mathbf{PM}\|\cdot\|\mathbf{U_M}-\mathbf{U_P}\|} dS$$

and is approximated in a discretized space (e.g. figure A.36) by:

$$\Gamma_2(P) = \frac{1}{N_p}\sum_S \frac{[\mathbf{PM}\wedge(\mathbf{U_M}-\mathbf{U_P})]\cdot\mathbf{z}}{\|\mathbf{PM}\|\cdot\|\mathbf{U_M}-\mathbf{U_P}\|}$$

Graftiaux et al. [20] have demonstrated that in the limit of a very small area S (S $\to$ 0) and for a two dimensional incompressible velocity field, Γ_2 is a local function depending only on:

- The rotation rate Ω expressed by the anti-symmetrical part of the velocity gradient tensor ∇u at P.
- The eigenvalue μ of the symmetrical part of the velocity tensor gradient ∇u at P.

The local character of the flow may be classified in function of $|\Omega/\mu|$. Table A.10 summarizes the flow specificities and associated $|\Gamma_2|$ values in function of $|\Omega/\mu|$.

$\|\Omega/\mu\| < 1$	flow locally dominated by strain	$\|\Gamma_2\| < 2/\pi$
$\|\Omega/\mu\| = 1$	pure shear	$\|\Gamma_2\| = 2/\pi$
$\|\Omega/\mu\| > 1$	flow locally dominated by rotation	$\|\Gamma_2\| > 2/\pi$

Table A.10: Flow properties according to $|\Gamma_2|$ values.

Observation of early results have shown the necessity of implementing some criteria concerning the vortex

centres location in order to detect only the vortices aligned with the trailing edge and corresponding to the Karman modes centred downstream of the trailing edge. Table A.11 reports the used criteria.

Minimum X distance from trailing edge	1 mm
Maximum Y distance from the wake centreline	3 mm
Minimum number of detected points	10

Table A.11: Vortex core centres detection criteria

Furthermore, vortices in contact with the boundaries of the domain have been automatically eludated by the detection algorithm. In order to keep only the vortices with a significant size, a minimum value of 10 points is composed for the cores detection.

References

[1] A. Bakhshandeh Rostami, M. Mobasher Amini, A. Fernandes, Strouhal number of flat and flapped plates at moderate reynolds number and different angles of attack: experimental data, Acta Mechanicadoi:10.1007/s00707-018-2292-2.

[2] J. M. Chen, Y.-C. Fang, Strouhal numbers of inclined flat plates, Journal of Wind Engineering and Industrial Aerodynamics 61 (2) (1996) 99–112. doi:https://doi.org/10.1016/0167-6105(96)00044-X.

[3] A. Stokes, M. Welsh, Flow-resonant sound interaction in a duct containing a plate, ii: Square leading edge, Journal of Sound and Vibration 104 (1986) 55–73. doi:10.1016/S0022-460X(86)80131-6.

[4] R. Parker, M. Welsh, Effects of sound on flow separation from blunt flat plates, International Journal of Heat and Fluid Flow 4 (2) (1983) 113–127. doi:https://doi.org/10.1016/0142-727X(83)90014-0.
URL https://www.sciencedirect.com/science/article/pii/0142727X83900140

[5] L. L. Shi, Y. Z. Liu, J. Yu, Piv measurement of separated flow over a blunt plate with different chord-to-thickness ratios, Journal of Fluids and Structures 26 (4) (2010) 644–657. doi:https://doi.org/10.1016/j.jfluidstructs.2010.02.001.
URL https://www.sciencedirect.com/science/article/pii/S0889974610000307

[6] Q. Zhang, Y. Liu, Influence of incident vortex street on separated flow around a finite blunt plate: Piv measurement and pod analysis, Journal of Fluids and Structures 55. doi:10.1016/j.jfluidstructs.2015.03.017.

[7] Y. Nakamura, Y. Ohya, H. Tsuruta, Experiments on vortex shedding from flat plates with square leading and trailing edges, Journal of Fluid Mechanics 222 (1991) 437–447.

[8] E. Naudascher, D. Rockwell, Flow-Induced Vibrations: An Engineering Guide, Routledge, 1994.

[9] R. MILLS, J. SHERIDAN, K. HOURIGAN, Particle image velocimetry and visualization of natural and forced flow around rectangular cylinders, Journal of Fluid Mechanics 478 (2003) 299–323. doi:10.1017/S0022112002003439.

[10] Z. J. Taylor, R. Gurka, G. A. Kopp, Effects of leading edge geometry on the vortex shedding frequency of an elongated bluff body at high reynolds numbers, Journal of Wind Engineering and Industrial Aerodynamics 128 (2014) 66–75. doi:https://doi.org/10.1016/j.jweia.2014.03.007.

[11] R. D. Blevins, Flow induced vibration of bluff structures, Ph.D. thesis, California Institut of Technology (1974).

[12] O. M. Griffin, S. E. Ramberg, The vortex-street wakes of vibrating cylinders, Journal of Fluid Mechanics 66 (3) (1974) 553–576. doi:10.1017/S002211207400036X.

[13] P. K. Stansby, The locking-on of vortex shedding due to the cross-stream vibration of circular cylinders in uniform and shear flows, Journal of Fluid Mechanics 74 (4) (1976) 641–665. doi:10.1017/S0022112076001985.

[14] P. W. Bearman, Vortex shedding from oscillating bluff bodies, Annual Review of Fluid Mechanics 16 (1) (1984) 195–222. doi:10.1146/annurev.fl.16.010184.001211.

[15] G. H. Toebes, P. S. Eagleson, Hydroelastic Vibrations of Flat Plates Related to Trailing Edge Geometry, Journal of Basic Engineering 83 (4) (1961) 671–678. doi:10.1115/1.3662292.

[16] A. Zobeiri, P. Ausoni, F. Avellan, M. Farhat, How oblique trailing edge of a hydrofoil reduces the vortex-induced vibration, Journal of Fluids and Structures 32 (2012) 78–89. doi:10.1016/j.jfluidstructs.2011.12.003.

[17] Z. Yao, F. Wang, M. Dreyer, M. Farhat, Effect of trailing edge shape on hydrodynamic damping for a hydrofoil, Journal of Fluids and Structures 51. doi:10.1016/j.jfluidstructs.2014.09.003.

[18] A. Zobeiri, Effect of hydrofoil trailing edge geometry on the wake dynamics, Ph.D. thesis, École Polytechnique Fédérale de Lausanne (2012).

[19] P. Ausoni, Turbulent vortex shedding from a blunt trailing edge hydrofoil, Ph.D. thesis, École Polytechnique Fédérale de Lausanne (2009).

[20] L. Graftieaux, M. Michard, N. Grosjean, Combining piv, pod and vortex identification algorithms for the study of unsteady turbulent swirling flows, Measurement Science and Technology 12 (2001) 1422. doi:10.1088/0957-0233/12/9/307.

[21] Vortex Induced Vibrations Analysis of a Cantilevered Blunt Plate by Proper Orthogonal Decomposition of TR-PIV and Structural Modal Analysis, Vol. Volume 2: Fluid Mechanics; Multiphase Flows of Fluids Engineering Division Summer Meeting, v002T03A050. doi:10.1115/FEDSM2020-20226.
URL https://doi.org/10.1115/FEDSM2020-20226

[22] L. Pernod, A. Ducoin, H. L. Sourne, J.-A. Astolfi, P. Casari, Experimental and numerical investigation of the fluid-structure interaction on a flexible composite hydrofoil under viscous flows, Ocean Engineering 194 (2019) 106647. doi:https://doi.org/10.1016/j.oceaneng.2019.106647.

[23] M. Raffel, C. Willert, S. Wereley, J. Kompenhans, Particle Image Velocimetry: A Practical Guide, 2007. doi:10.1007/978-3-540-72308-0.

[24] L. Sirovich, Turbulence and the dynamics of coherent structures. i - coherent structures. ii - symmetries and transformations. iii - dynamics and scaling, Quarterly of Applied Mathematics - QUART APPL MATH 45. doi:10.1090/qam/910463.

[25] G. Berkooz, P. Holmes, J. Lumley, The proper orthogonal decomposition in the analysis of turbulent flows, Annual Review of Fluid Mechanics 25 (2003) 539–575. doi:10.1146/annurev.fl.25.010193.002543.

[26] A. Chatterjee, An introduction to the proper orthogonal decomposition, Current Science 78.

[27] L. Cordier, M. Bergmann, Proper Orthogonal Decomposition: an overview, in: Lecture series 2002-04, 2003-03 and 2008-01 on post-processing of experimental and numerical data, Von Karman Institute for Fluid Dynamics, 2008., VKI, 2008, p. 46 pages.

[28] P. Holmes, J. L. Lumley, G. Berkooz, C. W. Rowley, Turbulence, Coherent Structures, Dynamical Systems and Symmetry, 2nd Edition, Cambridge Monographs on Mechanics, Cambridge University Press, 2012. doi:10.1017/CBO9780511919701.

[29] R. D. Blevins, Flow-induced vibration, Van Nostrand Reinhold Inc., 1977.

[30] C. Norberg, Flow around a circular cylinder: Aspects of fluctuating lift, Journal of Fluids and Structures 15 (2001) 459–469.

[31] Z. Taylor, E. Palombi, R. Gurka, G. Kopp, Features of the turbulent flow around symmetric elongated bluff bodies, Journal of Fluids and Structures 27 (2011) 250–265. doi:10.1016/j.jfluidstructs.2010.10.004.

[32] S. BALACHANDAR, R. MITTAL, F. M. NAJJAR, Properties of the mean recirculation region in the wakes of two-dimensional bluff bodies, Journal of Fluid Mechanics 351 (1997) 167–199. doi:10.1017/S0022112097007179.

[33] G. Chopra, S. Mittal, Drag coefficient and formation length at the onset of vortex shedding, Physics of Fluids 31 (2019) 013601. doi:10.1063/1.5075610.

[34] P. W. Bearman, Investigation of the flow behind a two-dimensional model with a blunt trailing edge and fitted with splitter plates, Journal of Fluid Mechanics 21 (2) (1965) 241–255. doi:10.1017/S0022112065000162.

[35] O. M. Griffin, A note on bluff body vortex formation, Journal of Fluid Mechanics 284 (1995) 217–224. doi:10.1017/S0022112095000322.

[36] L. S. G. Kovásznay, G. I. Taylor, Hot-wire investigation of the wake behind cylinders at low reynolds numbers, Proceedings of the Royal Society of London. Series A. Mathematical and Physical Sciences 198 (1053) (1949) 174–190. doi:10.1098/rspa.1949.0093.

[37] C. Williamson, R. Govardhan-Ankulkar, A brief review of recent results in vortex-induced vibrations, Journal of Wind Engineering and Industrial Aerodynamics 96 (2008) 713–735.

[38] B. Oudheusden, F. Scarano, N. Van Hinsberg, D. Watt, Phase-resolved characterization of vortex shedding in the near wake of a square-section cylinder at incidence, Experiments in Fluids 39 (2005) 86–98. doi:10.1007/s00348-005-0985-5.

[39] T. P. Miyanawala, R. K. Jaiman, Decomposition of wake dynamics in fluid–structure interaction via low-dimensional models, Journal of Fluid Mechanics 867 (2019) 723–764. doi:10.1017/jfm.2019.140.

[40] Q. Zhang, Y. Liu, Separated flow over blunt plates with different chord-to-thickness ratios: Unsteady behaviors and wall-pressure fluctuations, Experimental Thermal and Fluid Science 84 (2017) 199–216. doi:https://doi.org/10.1016/j.expthermflusci.2017.02.007.
URL https://www.sciencedirect.com/science/article/pii/S0894177717300365

[41] R. Hu, Y. Liu, Proper orthogonal decomposition of turbulent flow around a finite blunt plate, Journal of Visualization 21. doi:10.1007/s12650-018-0496-0.

[42] N. J. Cherry, R. Hillier, M. E. M. P. Latour, Unsteady measurements in a separated and reattaching flow, Journal of Fluid Mechanics 144 (1984) 13–46.

[43] S. Kaneko, T. Nakamura, F. Inada, M. Kato, Flow-Induced Vibrations: Classifications and Lessons from Practical Experiences: Second Edition, Elsevier, 2008.

[44] A. Sevilla, C. Martínez-Bazán, Vortex shedding in high reynolds number axisymmetric bluff-body wakes: Local linear instability and global bleed control, Physics of Fluids - PHYS FLUIDS 16 (2004) 3460–3469.

[45] T. L. MORSE, C. H. K. WILLIAMSON, Prediction of vortex-induced vibration response by employing controlled motion, Journal of Fluid Mechanics 634 (2009) 5–39. doi:10.1017/S0022112009990516.

[46] M. Michard, L. Graftieaux, L. Lollini, N. Grosjean, Identification of vortical structures by a non-local criterion: Applications to p.i.v. measurements ans d.n.s results of turbulent rotating flows, Eleventh Symposium on Turbulent Shear Flows, Grenoble, 1997.

Nomenclature

Abbreviations

$ILEV$	impinging leading edge vortex
KVS	Karman vortex shedding
LSB	laminar separation bubble
PIV	particle image velocimetry
POD	proper orthogonal decomposition
SL	shear layer
$SLVS$	shear layer vortex shedding
TEI	trailing edge instability
TKE	turbulent kinetic energy
WB	wake bubble

Greek symbols

Γ	vortex circulation [$m^2.s^{-1}$]
λ_{vs}	vortex shedding wave length [m]
ν	kinematic viscosity [$m^2.s^{-1}$]
Ω	vortex rotation rate [s^{-1}]
Φ_k	spatial function of POD mode k [−]
ρ	fresh water density [$kg.m^3$]

Latin symbols

$\bar{U}$	averaged horizontal velocity component [$m.s^{-1}$]
$\bar{V}$	averaged vertical velocity component [$m.s^{-1}$]
A	vortex area [m^2]
a_k	time coefficient of POD mode k [−]
a_n^{rms}	root mean square of time coefficient of POD mode k [−]
c	plate chord [m]
C_D	drag coefficient [−]
C_L	lift coefficient [−]
D	plate thickness [m]
f_1	first bending mode natural frequency [Hz]
f_2	first twisting mode natural frequency [Hz]
f_3	second bending mode natural frequency [Hz]
f_f	flapping frequency [Hz]
f_R	characteristic frequency of laminar separation bubble [Hz]
f_s^{max}	frequency of highest amplitude of vibration velocity spectrum [Hz]
f_{vs}	vortex shedding frequency [Hz]
L	characteristic length [m]
L_e	vortex formation length [m]
L_R	length of laminar separation bubble [m]
M	mass of the plate [kg]
$N_{90\%}$	number of modes to reach 90 % of TKE [−]
Re_c	chord based Reynolds number [−]
Re_D	thickness based Reynolds number [−]
Re_L	characteristic length L based Reynolds number [−]
RU_n	reduced velocity based on natural frequency n [−]
s	plate span [m]
St_c	chord based Strouhal number [−]
St_D^f	Strouhal based on flapping frequency [−]
St_L	characteristic length L based Strouhal number [−]
St_R	Strouhal based on laminar separation bubble frequency and length [−]
St_{DR}	Strouhal based on laminar separation bubble frequency and plate thickness [−]
u	horizontal velocity component [$m.s^{-1}$]
u'	fluctuating horizontal velocity component [$m.s^{-1}$]
U_0	free stream velocity [$m.s^{-1}$]
U_Φ	phase velocity [$m.s^{-1}$]
U_{defect}	velocity deficit [$m.s^{-1}$]
v	vertical velocity component [$m.s^{-1}$]
v'	fluctuating vertical velocity component [$m.s^{-1}$]
V_s^{max}	highest amplitude of vibration velocity spectrum [$m.s^{-1}$]
V_s^{rms}	root mean square of vibration velocity signal [$m.s^{-1}$]